# Towards a holistic understanding of blocked regime dynamics through a combination of complementary diagnostic perspectives

Seraphine Hauser[1], Franziska Teubler[2], Michael Riemer[2], Peter Knippertz[1], and Christian M. Grams[1]

[1]Institute of Meteorology and Climate Research (IMK-TRO), Department Troposphere Research, Karlsruhe Institute of Technology (KIT), Karlsruhe, Germany

[2]Institute for Atmospheric Physics, Johannes Gutenberg-University Mainz, Mainz, Germany

**Correspondence:** Seraphine Hauser (seraphine.hauser@kit.edu)

**Abstract.** Atmospheric blocking describes a situation in which a stationary and persistent anticyclone blocks the eastward propagation of weather systems in the midlatitudes and can lead to extreme weather events. In the North Atlantic-European region blocking contributes to life cycles of weather regimes, which are recurrent, quasi-stationary, and persistent patterns of the large-scale circulation. Despite progress in blocking theory over the last decades, we are still lacking a comprehensive, process-based conceptual understanding of blocking dynamics. Here we combine three different perspectives on so-called 'blocked' weather regimes, namely the commonly used Eulerian and Lagrangian perspectives, complemented by a novel quasi-Lagrangian perspective. Within the established framework of mid-latitude potential vorticity (PV) thinking, the joint consideration of the three perspectives enables a comprehensive picture of the dynamics and quantifies the importance of dry and moist processes during a blocked weather regime life cycle.

We apply the diagnostic framework to a European Blocking weather regime life cycle in March 2016, which was associated with a severe forecast bust in the North Atlantic-European region. The three perspectives highlight the importance of moist processes during the onset or maintenance of the blocked weather regime. The Eulerian perspective, which identifies the processes contributing to the onset and decay of the regime, indicates that dry quasi-barotropic wave dynamics and especially the eastward advection of PV anomalies (PVAs) into the North Atlantic-European ~~sector~~ region dominate the onset of the regime pattern. By tracking the negative upper-tropospheric PVA associated with the 'block', the quasi-Lagrangian view reveals, for the same period, abrupt amplification due to moist processes. This is in good agreement with the Lagrangian perspective indicating that a large fraction of air parcels that end up in the negative PVA experiences diabatic heating. Overall, the study shows that important contributions to the development take place outside of the region in which the blocked weather regime eventually establishes, and that a joint consideration of different perspectives is important in order not to miss processes, in particular moist-baroclinic dynamics, contributing to a blocked regime life cycle.

## 1 Introduction

Atmospheric blocking is a phenomenon in the mid and high latitudes where stationary, long-lived high pressure systems disrupt the mean westerly flow and 'block' the propagation of weather systems (e.g. Rex, 1950; Steinfeld and Pfahl, 2019). Thereby,

blocking does not only mean the block itself but also the circulation pattern in which the block forms the dominant part, such that blocking can be considered from the perspective of so-called weather regimes. These large-scale, quasi-stationary and recurrent atmospheric circulation states make up an important part of the extratropical atmospheric variability on intraseasonal time scales (Vautard, 1990; Michelangeli et al., 1995; Cassou, 2008). Low-frequency circulation regimes affect continent-size regions for several days and modulate the location and intensity of synoptic-scale weather systems that determine surface weather (Yiou and Nogaj, 2004). The weather regimes that are dominated by an anticyclonic circulation anomaly which essentially is also identified as atmospheric blocking are here referred to as 'blocked' regimes. ~~Low-frequency circulation regimes affect continent-size regions for several days and modulate the location and intensity of synoptic-scale weather systems that determine surface weather (Yiou and Nogaj, 2004).~~ Due to their stationarity, these regimes can regionally lead to extreme weather events (Kautz et al., 2022), such as flooding (Houze et al., 2011; Hong et al., 2011), heat waves and associated droughts (Pfahl and Wernli, 2012; Lavaysse et al., 2018; Alvarez-Castro et al., 2018), cold spells (Sillmann et al., 2011; Buehler et al., 2011; Ferranti et al., 2018), and storms (Donat et al., 2010; Grams et al., 2017). In terms of predictability, weather regimes have an undisputed importance in forecasting, as they shape the sub-seasonal 'predictability desert' between medium-range and seasonal forecasts (Vitart et al., 2012; Cortesi et al., 2021). Enhanced predictability may be expected for regimes that feature prominent anticyclonic circulation anomalies because, once established, anticyclonic anomalies exhibit slower decay rates than cyclonic anomalies, suggesting a self-sustaining nature of anticyclonic anomalies (e.g. Shutts, 1983). However, state-of-the-art numerical weather prediction models struggle with the correct representation of regimes dominated by anticyclonic anomalies where especially the onset and maintenance of the 'blocked' circulation pattern pose a difficulty (Ferranti et al., 2015; Matsueda and Palmer, 2018; Grams et al., 2018).

Existing studies on the dynamics of blocked circulation patterns address various aspects of a blocking life cycle using different approaches and addressing different spatial and temporal scales: Important processes on large scales are wave dynamics (Austin, 1980), wave resonance to a given forcing (Petoukhov et al., 2013), the role of topography in the initiation of blocking on the planetary scale (Charney and DeVore, 1979; Grose and Hoskins, 1979), and the impact of tropical heating (Henderson et al., 2016). A notable study in this context by Nakamura and Huang (2018) discusses the onset of a block by the convergence and the subsequent constrained zonal propagation of wave activity as a jet stream 'traffic jam'. On smaller spatial scales, studies have found an effect of enhanced transient activity (Nakamura and Wallace, 1990) and especially the role of upstream cyclones by the transfer of vorticity and momentum to the block (Nakamura and Wallace, 1993). However, it is not only the individual mechanisms at different scales ~~,~~ but the scale interaction that is of importance for the onset and the blocking maintenance stage (e.g., Shutts, 1983; Nakamura et al., 1997; Luo et al., 2014; Miller and Wang, 2022). For example, one theory for maintaining a block by the interplay of different scales is based on the idea that an existing mature block absorbs smaller-scale eddies of the same polarity and thus re-enforces itself (Yamazaki and Itoh, 2009). While the theories described above are more related to the 'dry' dynamics, studies in recent years emphasize the importance of moist-diabatic processes in modifying the midlatitude flow in the upper troposphere (Grams et al., 2011; Pfahl et al., 2015; Steinfeld and Pfahl, 2019; Teubler and Riemer, 2021). Warm conveyor belts (WCBs) – rapidly ascending airstreams in the vicinity of extratropical cyclones - play an important role

here, because latent heat release in the midlatitudes occurs mostly within WCBs, and WCBs transport low-tropospheric air to the upper troposphere leading to divergent outflow near the tropopause (Wernli, 1997; Madonna et al., 2014; Pfahl et al., 2015; Steinfeld and Pfahl, 2019). All the studies mentioned above handle different mechanisms of blocking dynamics and contribute to a significant progress in diverse blocking dynamic theories. However, so far the individual mechanisms have not been considered together to get a complete, comprehensive picture of the blocking dynamics (Lupo, 2021).

In this study, we make use of potential vorticity (PV; Rossby, 1940; Hoskins et al., 1985) as a key variable in atmospheric dynamics ~~in order~~ to capture the balanced dynamics of regimes. Low PV air masses are advected poleward during blocking, leading to anticyclonic anomalies in the upper troposphere associated with a meridional amplification of Rossby waves. Teubler and Riemer (2016, 2021) have developed a quantitative framework based on Ertel PV (Ertel, 1942) that allows the decomposition of the total change in PV into different processes that contribute to the evolution of upper-tropospheric PV anomalies (PVAs) associated with Rossby wave packets (Wirth et al., 2018a). ~~They distinguish~~ A piecewise PV inversion is performed in Teubler and Riemer (2021) in order to separately consider the influence of baroclinic interaction and quasi-baroclinic propagation. The consequent distinction between quasi-barotropic, baroclinic, divergent, and non-conservative PV tendencies ~~, which allows quantifying the effect of~~ allows the quantification of the effects associated with dry and moist dynamics on the amplitude evolution of troughs and ridges. *Quasi-barotropic* PV tendencies are associated with upper-tropospheric linear wave dynamics and describe the advection of PVAs by the background flow and the advection of background PV by the flow associated with PVAs (intrinsic wave propagation). The impact of lower-tropospheric PVAs on upper-tropospheric PVAs is described by *baroclinic* PV tendencies. *Divergent* PV tendencies are due to PV advection by the divergent wind, which incorporates the impact of WCB outflow on upper-tropospheric PV. The direct impact of diabatic processes on the PV distribution is represented by *non-conservative* PV tendencies.

The setup of diagnostics in this study consists of three complementary approaches ~~in order~~ to look at blocking dynamics from various perspectives and to distinguish between identified mechanisms from previous studies on different temporal and spatial scales (~~Fig.~~Figure 1). Most importantly, we here consider blocking from the viewpoint of blocked weather regimes, i.e. regime ~~pattern~~ patterns with dominating anticyclonic circulation anomalies. ~~We therefore~~ Therefore, we use a year-round weather regime classification in the North Atlantic-European region by Grams et al. (2017). The first perspective – referred to as 'Eulerian' perspective in the following – is methodologically related to the well-known weather regime thinking, in which projections of a current field onto a mean regime field are used to obtain life cycles of weather regimes (Michel and Rivière, 2011; Grams et al., 2017). Several studies in the past have looked at regime dynamics and especially the transition phases with a low-frequency ~~streamfunction~~ stream function budget to quantify the processes involved (Benedict et al., 2004; Feldstein, 2003; Michel and Rivière, 2011). We here translate this Eulerian approach to PV, by considering the projection of low-frequency PVAs and PV tendencies onto a mean regime pattern. ~~This~~ The projection of the anomaly's tendency is equivalent to the tendency of the projection of the anomaly and thus enables the quantification of processes leading to the onset and decay of the full regime pattern (~~Fig.~~Figure 1a). Next, we exclusively trace the anticyclonic, upper-tropospheric PVAs

associated with the dominant anticyclonic circulation anomaly of a blocked weather regime pattern. This "quasi-Lagrangian" approach is strongly leaning on the blocking identification method of Schwierz et al. (2004) based on upper-tropospheric anticyclonic PV anomalies. A new objective tracking algorithm, which detects and quantifies the effect of splitting and merging of PVAs, enables an integrated investigation of the selective absorption mechanism by Yamazaki and Itoh (2009) mentioned above. The PV framework of Teubler and Riemer (2016) was originally used for ridges and troughs (identified as negative and positive PVAs) within a Rossby wave packet and is ~~now generally~~ here applied to upper-tropospheric negative PVAs to quantify the processes associated with the PVA amplitude change (~~Fig.~~Figure 1b). The quasi-Lagrangian perspective allows us to determine the origin of PVAs that evolve into blocking anticyclones and, for the first time, to determine the contribution of dry and moist dynamics to the amplitude evolution of PVAs using piecewise PV tendencies. The third perspective is Lagrangian in nature and is based on trajectory thinking, which has been used in studies by Pfahl et al. (2015) and Steinfeld and Pfahl (2019) to investigate the air masses associated with blocking. By calculating backward trajectories of air parcels from blocking anticyclones, it is possible to investigate how these negative upper-tropospheric PVAs have been created and if diabatic heating and therefore 'moist' dynamics have played an important role (~~Fig.~~Figure 1c).

The purpose of this study is to demonstrate how, by combining the three perspectives, a holistic view ~~on~~ of the dynamical evolution of a blocked regime life cycle can be achieved. We use a European Blocking (EuBL) regime life cycle in March 2016, which was sensitive to moist-baroclinic development during the onset stage (Magnusson, 2017; Grams et al., 2018), as an illustrative case study. The paper is organized as follows: ~~Sect.~~Section 2 introduces the data sets and provides a detailed overview of the three different perspectives that are combined in this study. The EuBL life cycle in March 2016 is presented in ~~Sect.~~Section 3 with a brief description of the evolution of the larger-scale flow. ~~Sect.~~Section 4 presents the PV dynamics from the three different perspectives (Eulerian, quasi-Lagrangian, and Lagrangian) applied to the case study from ~~Sect.~~Section 3. The discussion of the complementary perspectives and a comparison with previous literature ~~is content of Sect.~~constitutes the content of Section 5. The study closes with the main conclusions and an outlook in ~~Sec.~~Section 6.
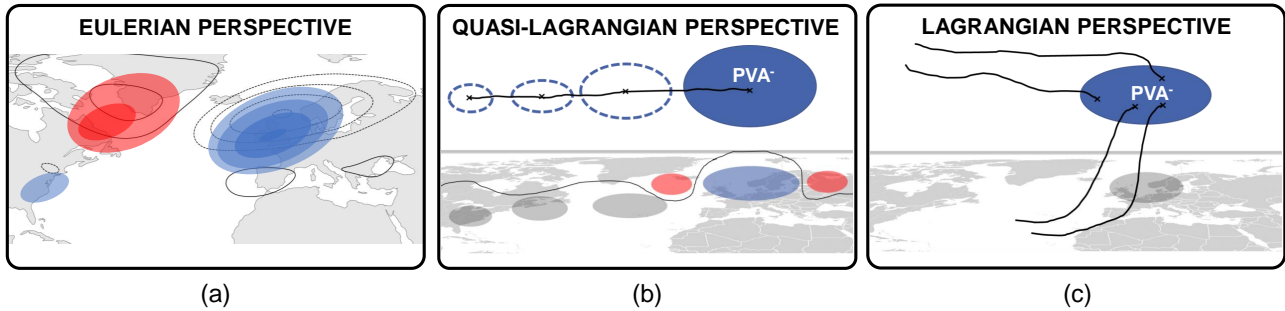
**Figure 1.** ~~Schematic overview of the three perspectives on the PV dynamics of blocked weather regime life cycles~~Schematic overview of the three perspectives on the PV dynamics of blocked weather regime life cycles. (a) The Eulerian perspective quantifies the PV dynamics by projecting different upper-tropospheric PV tendency terms onto the mean regime pattern. Black solid (dashed) contours schematically show the PV pattern for the EuBL regime and therefore the location of positive and negative upper-tropospheric PVAs. Red ~~(and~~ blue ~~)~~ shading shows exemplary positive ~~(and~~ negative ~~)~~ PVAs at a fixed point in time, respectively. (b) The quasi-Lagrangian perspective follows negative upper-tropospheric PVAs, assigns them to active regime life cycles, and investigates the PVA amplitude evolution. The solid black line connects the center of ~~masses~~ mass positions of PVA objects (shown as blue dashed contours for different times) and points to the negative PVA track. Note that the tracked negative PVA is part of ~~an~~ a Rossby wave packet as displayed by the sequence of negative (blue shading) and positive (red shading) PVAs. The thin black line on the map shows schematically the position of the ~~wave guide~~waveguide. (c) The Lagrangian perspective calculates backward trajectories out of the negative PVA ~~from~~ defined in the quasi-Lagrangian perspective in (b) and focuses on the diabatic and non-diabatic history of air parcels that end up in the negative PVA. Black lines represent schematically backward trajectories from a negative PVA (starting points marked with a black cross).

## 2 Data and Methods

### 2.1 Data

120 This study is based on the reanalysis data set ERA5 of the European Centre for Medium-Range Weather Forecasts (ECMWF), which is available from 1950 to the present (Hersbach et al., 2020). We use data for the period January 1, 1979 – December 31, 2019, remapped from the original T639 spectral resolution to a regular latitude-longitude grid. For the identification of upper-tropospheric PVAs in the quasi-Lagrangian approach, we select ERA5 model level data for maximum possible vertical resolution, with a temporal resolution of 3 hours and a horizontal grid spacing of $0.5°$. We use spatially coarser data ($1°$) for the

125 PV inversion, also with 3-hourly resolution and with 17 pressure levels (1000, 950, 925, 900, 850, 800, 700, 600, 500, 400, 300, 250, 200, 150, 100, 70, and $50\,\mathrm{hPa}$). Mean temperature and wind tendencies at model levels from ERA5 short-range forecasts serve to estimate non-conservative processes with a spatial resolution of $0.5°$ in the horizontal and a temporal resolution of 1 hour. ERA5 provides these tendencies accumulated over the previous hour, from which we calculate a 3-hourly mean around analysis time (e.g. taking the mean of data valid at 2, 3 and $4\,\mathrm{UTC}$ for the analysis at $3\,\mathrm{UTC}$). We here distinguish between

130 tendencies from all parameterizations and non-radiative parameterizations.

## 2.2 PV framework: Quantification of individual processes

This work uses Ertel's PV as q = $\sigma^{-1}(\zeta_\theta + f)$ (Ertel, 1942) in its hydrostatic approximation on isentropic levels, where $\zeta_\theta$ is the component of relative vorticity perpendicular to an isentropic surface, $f$ the Coriolis parameter and $\sigma = -g^{-1}(\partial p/\partial \theta)$ the isentropic layer density with gravity $g$, pressure $p$, and potential temperature $\theta$. The PV tendency equation is given by isentropic advection and non-conservative PV modification ($\mathcal{N}$):

$$\left.\frac{\partial q}{\partial t}\right|_\theta = -\boldsymbol{v}\cdot\boldsymbol{\nabla}_\theta q + \mathcal{N}, \tag{1}$$

with $\boldsymbol{v} = (u,v,0)$ the ~~horizontal isentropic~~ wind vector and $\boldsymbol{\nabla}_\theta$ the gradient operator along an isentropic surface. The non-conservative PV modification is given by

$$\mathcal{N} = -\dot{\theta}\frac{\partial q}{\partial \theta} + \frac{1}{\sigma}\left[(\boldsymbol{\nabla}_\theta \times \boldsymbol{v} + f\boldsymbol{k})\cdot\boldsymbol{\nabla}_\theta\dot{\theta} + \boldsymbol{k}\cdot(\boldsymbol{\nabla}_\theta \times \dot{\boldsymbol{v}})\right], \tag{2}$$

with $\boldsymbol{k} = (0,0,1)$ the unit vector perpendicular to an isentropic surface, $\dot{\theta}$ the non-conservative heating rate, and $\dot{\boldsymbol{v}}$ the sources and sinks of non-conservative momentum ~~.~~ (e.g., friction or gravity wave drag). We estimate the non-conservative PV modification term $\mathcal{N}$ with the mean 3-hourly temperature and wind tendencies introduced in ~~Sect.~~ Section 2.1.

The advection term in ~~Eq.~~ Equation 1 is ~~now~~ further separated into different processes (Hoskins et al., 1985; Teubler and Riemer, 2021). PVAs (~~mathematical expression used here:~~ $q'$) are defined as deviations from a climatological background state $q_0$ ~~constructed by daily averages from January 1980–December 2019 and filtered by~~ such that $q' = q - q_0$ is valid. For each time step within the year (recall $\Delta t = 3\,\text{h}$), averages are constructed based on the period from 1980–2019. This is used for the climatological background state $q_0$ defined as a 30-day running mean climatology centered on the respective time to ensure smooth transitions ~~between~~ in $q_0$ between consecutive time steps. Following the basics of PV thinking, the three-dimensional distribution of PVAs can be further separated into upper-tropospheric and lower-tropospheric PV (and temperature) anomalies ~~to represent Rossby wave packets and upper-tropospheric large-scale anomalies like blocking, and cyclones and baroclinic waves, respectively (Davis et al., 1996; Teubler and Riemer, 2016)~~. Here, the separation level of upper-tropospheric and lower-tropospheric PV anomalies lies between 600 and 650 hPa. Piecewise PV inversion with the non-divergent wind field under nonlinear balance (Charney, 1955; Davis and Emanuel, 1991; Davis, 1992) is performed on pressure levels between 25 °N and 80 °N and yields the wind fields ~~$\boldsymbol{v}_{up}$ and $\boldsymbol{v}_{low}$~~ $\boldsymbol{v}'_{up}$ and $\boldsymbol{v}'_{low}$ associated with the upper-tropospheric and lower-tropospheric PV anomalies, respectively. It is important to note that our quantitative analysis is performed for the evolution of upper-tropospheric anomalies. From the PV perspective of midlatitude dynamics, we may thus consider the impact of the upper-tropospheric anomalies on themselves (mediated by $\boldsymbol{v}'_{up}$) as quasi-barotropic dynamics, and the impact of the lower-tropospheric anomalies on the upper-tropospheric anomalies (mediated by $\boldsymbol{v}'_{low}$) as baroclinic dynamics. The piecewise PV inversion thus provides the possibility to consider the influence of the dynamics in the lower troposphere and the influence of the wave on itself, separately from each other. ~~A detailed documentation with all selected thresholds for the PV inversion can be found in Teubler and Riemer (2021)~~ The background wind field $\boldsymbol{v}_0$ is obtained in the same way as the background PV field

$q_0$ as a 30-day running mean climatology (1980–2019) centered on the respective calendar day, and is in good approximation balanced. Per definition, the wind fields ~~$v_{up}$ and $v_{low}$~~ $v'_{up}$ and $v'_{low}$ from piecewise PV inversion are non-divergent and will

165 hence be further complemented by the divergent flow ~~$v_{div}$~~ $v'_{div}$. All wind fields are interpolated to isentropic levels. Following Röthlisberger et al. (2018), we select an isentropic level average around 320 K (namely 315, 320, and 325 K) for the EuBL in March 2016. The full wind field can finally be divided into:

$$\boldsymbol{v} = \boldsymbol{v}_0 + \boldsymbol{v}' = \boldsymbol{v}_0 + \boldsymbol{v}'_{\underline{rot}\,\underline{div}} + \boldsymbol{v}_{\underline{div}\,\underline{rot}}' = \boldsymbol{v}_0 + \boldsymbol{v}'_{\underline{div}} + \boldsymbol{v}'_{up} + \boldsymbol{v}'_{low} + \boldsymbol{v}_{\underline{div}+}{}'_{res}. \tag{3}$$

We introduce here the residual ~~$v_{res}$~~ $v'_{res}$, which arises due to (i) characteristics inherent in piecewise PV inversion, e.g., nonlin-

170 earities and imperfect knowledge of boundary conditions, (ii) numerical inaccuracies and (iii) the interpolation of wind fields from pressure to isentropic levels. A more detailed discussion of the PV partitioning, the piecewise PV inversion technique, and the residual is given in Teubler and Riemer (2021).

With the partitioning of PV into a background state and anomalies thereof, and the associated partitioning of the wind field,

175 a PV-anomaly tendency equation can be written following ~~Eq.~~ Equation 1 as:

$$\begin{aligned}
\frac{\partial q'}{\partial t} &= \frac{\partial q}{\partial t} - \frac{\partial q_0}{\partial t} \\
&= \frac{\partial q'}{\partial t}\bigg|_{qb} + \frac{\partial q'}{\partial t}\bigg|_{bc} + \frac{\partial q'}{\partial t}\bigg|_{div} + \frac{\partial q'}{\partial t}\bigg|_{eddy} + \frac{\partial q'}{\partial t}\bigg|_{noncons} + \frac{\partial q'}{\partial t}\bigg|_{res} \\
&= -\left[\boldsymbol{v}'_{up}\cdot\boldsymbol{\nabla} q_0 + \boldsymbol{v}_0\cdot\boldsymbol{\nabla} q'\right] - \boldsymbol{v}'_{low}\cdot\boldsymbol{\nabla} q_0 - \boldsymbol{v}'_{div}\cdot\boldsymbol{\nabla} q - \boldsymbol{\nabla}\cdot(\boldsymbol{v}'_{rot}q') + \mathcal{N} - \left[\boldsymbol{v}'_{res}\cdot\boldsymbol{\nabla} q_0 + \frac{\partial q_0}{\partial t} + \boldsymbol{v}_0\cdot\boldsymbol{\nabla} q_0\right],
\end{aligned} \tag{4}$$

where we have included in the residual term the (very small) tendencies due to our use of a slowly varying background state.

The first term (in square brackets) describes the PV thinking of (upper-tropospheric, linear) barotropic Rossby waves

180 (Hoskins et al., 1985; Wirth et al., 2018a), hereafter referred to as quasi-barotropic PV tendency. For a linear wave in uniform background flow, both individual contributions to this tendency are in quadrature with the PVAs, but with opposite ~~sign~~ signs. The first contribution (~~$v_{up}\cdot\boldsymbol{\nabla} q_0$~~ $v'_{up}\cdot\boldsymbol{\nabla} q_0$) represents intrinsic (phase and group) propagation, including the downstream development and amplification of anomalies at the leading edge of a Rossby wave packet. The second contribution ($\boldsymbol{v}_0\cdot\boldsymbol{\nabla} q'$) represents the Doppler shift, i.e., the advection of the wave pattern by the background flow. In a background flow with hor-

185 izontal shear, this term contributes to the deformation of PVAs. The second term in ~~Eq.~~ Equation 4 (~~$v_{low}\cdot\boldsymbol{\nabla} q_0$~~ $v'_{low}\cdot\boldsymbol{\nabla} q_0$) describes baroclinic interaction with lower-tropospheric PVAs, which leads on average to baroclinic growth, i.e., the amplification of upper-tropospheric ridge and trough anomalies (e.g. Teubler and Riemer, 2021). This term will hereafter be referred to as baroclinic PV tendency. The third term describes the impact of the divergent flow (hereafter referred to as divergent PV tendency). It is difficult to accurately attribute this divergent flow to individual processes, e.g., dry balanced dynamics vs. moist

190 processes. It is usually most reasonable, however, to attribute large values of the divergent PV tendency near the tropopause to latent heat release, which invigorates mid-tropospheric ascent and hence divergent outflow aloft. A more detailed discussion

of this issue can be found in Wirth et al. (2018a) and Teubler and Riemer (2021). In the current study, we verify this relationship explicitly using trajectory calculations. The fourth term in ~~Eq.~~ Equation 4 describes the nonlinear redistribution of PVAs in terms of the convergence of PVA flux by the (anomalous) rotational wind ($\nabla \cdot (v'_{rot}q')$ $\nabla \cdot (\boldsymbol{v}'_{rot}q')$), hereafter referred to simply as eddy flux convergence. Note that eddy flux convergence may change PVAs locally but may neither generate new nor amplify existing PVAs in a globally averaged sense (~~(~~because the flux vanishes at the boundary of the global domain). Furthermore, eddy flux convergence may not change the area-integrated amplitude of PVAs that are defined by a boundary at which $q' = 0$ (Teubler and Riemer, 2016). The fifth term ($\mathcal{N}$) depicts the direct non-conservative PV modification and contains all non-conservative processes, like latent heat release, friction, and radiation.

In the later ~~Sects.~~ Sections 2.4 and 2.5, our description of the evolution of PVAs associated with the dynamics of blocked weather regimes in the Eulerian and quasi-Lagrangian perspectives will build on the tendency in ~~Eq.~~ Equation 4.

## 2.3 Weather regimes in the North Atlantic-European region

In this study, we use the year-round definition of seven weather regimes in the North Atlantic-European region (NAE; 80 °W–40 °E, 30 °–90 °N; dashed gray in ~~Fig.~~ Figure 2a) by Grams et al. (2017) adapted to ERA5. Geopotential height anomalies are calculated based on a 90-day running mean climatology 1979–2019 at $500\,\mathrm{hPa}$ with a temporal resolution of 6 hours. Anomalies are additionally filtered by a 10-day low-pass filter (Lanczos Filter; Duchon, 1979) to exclude high-frequency signals. After ~~a~~ normalization of the anomalies for a year-round definition, k-means clustering is performed for the expanded phase space of the leading seven empirical orthogonal functions that describe $74.4\,\%$ of the variability. A weather regime is then defined as the cluster mean of one of seven clusters, which was shown to be the optimal number in the year-round definition. The seven weather regimes consist of three cyclonic regime types (Zonal regime - ZO, Scandinavian Trough - ScTr, Atlantic Trough - AT) and four anticyclonic regime types (Atlantic Ridge - AR, European Blocking - EuBL, Scandinavian Blocking - ScBL, Greenland Blocking - GL). In this study, we apply different methods to quantify weather regime dynamics to ~~an~~ a EuBL regime life cycle. The mean year-round regime pattern for EuBL is shown in ~~Fig.~~ Figure 2a. A positive geopotential height anomaly over the eastern north Atlantic and Europe dominates the regime pattern and is flanked by two areas of negative geopotential height anomalies upstream over Greenland and downstream over the Mediterranean and East Asia.

To make a quantitative statement about the similarity of an instantaneous pattern to the seven weather regimes, we use the weather regime index ($I_{WR}$) (Michel and Rivière, 2011; Grams et al., 2017) defined as

$$I_{WR}(t) = \frac{P_{WR}(t) - \overline{P_{WR}}}{\sqrt{\frac{1}{NT}\sum_{t=1}^{NT}[P_{WR}(t) - \overline{P_{WR}}]^2}} \qquad \text{with} \qquad P_{WR}(t) = \frac{\sum_{(\lambda,\varphi) \in NH} \Phi^L(t,\lambda,\varphi)\Phi_{WR}^L(\lambda,\varphi)\cos\varphi}{\sum_{(\lambda,\varphi) \in NH} \cos\varphi}, \qquad (5)$$

where NT is the total number of time steps within a climatological sample (all times in 1979–2019), $\overline{P_{WR}}$ the climatological mean of the projection $P_{WR}$, $\Phi^L(t,\lambda,\varphi)$ the low-frequency geopotential height anomaly at 500 hPa, $\Phi_{WR}^L$ the low-frequency geopotential height pattern that defines the weather regime, and $(\lambda,\varphi)$ the respective longitude/latitude on the northern hemi-
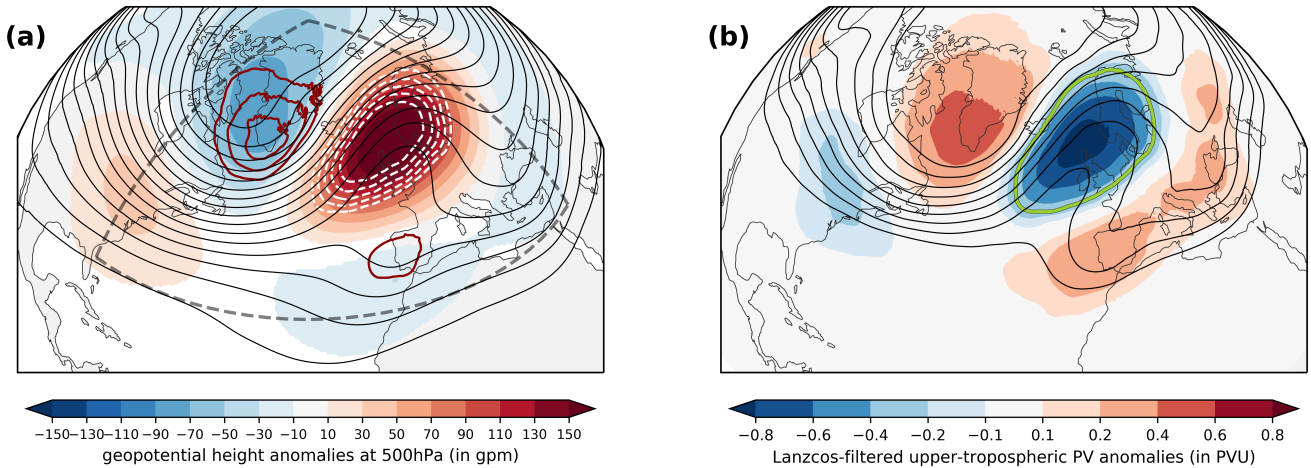
**Figure 2.** ~~Year-round weather regime composite of EuBL after Grams et al. (2017) based on geopotential height at 500 hPa and upper-tropospheric PV.~~ Year-round weather regime composite of EuBL after Grams et al. (2017) based on geopotential height at 500 hPa and upper-tropospheric PV. (a) Lanczos-filtered (10-days) geopotential height anomalies at 500 hPa (shading, in gpm), absolute geopotential height at 500 hPa (black lines every 40 gpm) and vertically-averaged PVAs between 500–150 hPa for negative (positive) values in dashed white (solid dark red) lines between 0.3 and 0.7 every 0.1 for all time steps attributed to the EuBL regime type (in PVU). The box (dashed gray) shows the area used to define the year-round weather regimes. (b) Lanczos-filtered (10-days) vertically-averaged PVAs between 500–150 hPa (shading) and vertically-averaged PV for all time steps attributed to the EuBL regime type (contours, in PVU, from 1.5 to 3.5 PVU in steps of 0.25 PVU). The bright green solid line illustrates the regime mask for the EuBL regime type, defined by the -0.3 PVU PVA contour.

sphere (NH).

225

Objective weather regime life cycles are derived based on the $I_{WR}$ for each regime and time step. Following Grams et al. (2017) a regime life cycle is defined as a persistent $I_{WR}$ above 1.0 for more than five consecutive days that shows for at least one time step the highest $I_{WR}$ in all seven regimes. A weather regime life cycle is called active ~~,~~ if the $I_{WR}$ lies above 1.0, and the first time step at which $I_{WR}$ > 1.0 is defined as the onset of the life cycle. The decay is then set as the first time at which the $I_{WR}$ is below 1.0 again. The course of the weather regime index around the EuBL life cycle in March 2016 is shown in ~~Fig.~~ Figure 3.

### 2.4 Eulerian PV perspective on the weather regime evolution

We are interested in the processes governing the dynamics of the EuBL in March 2016 from a PV perspective. Because EuBL is defined in terms of a low-frequency anomaly pattern (~~Sect.~~Section 2.3), we here apply the same 10-day low-pass filter to the PVAs, hence considering low-frequency PVAs $q^L$. Following, e.g., Feldstein (2003) and Michel and Rivière (2011), who studied the ~~streamfunction~~ stream function evolution of low-frequency modes like the North Atlantic Oscillation, we define a
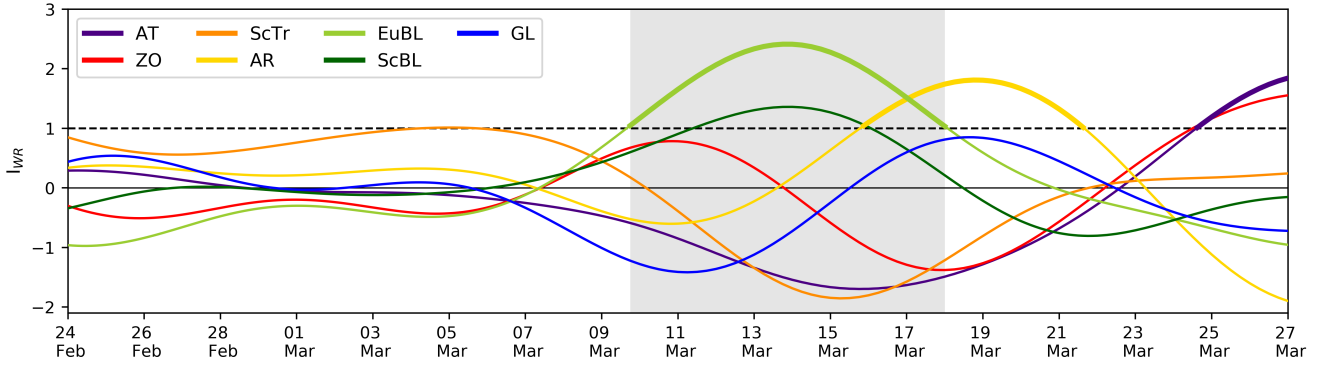
**Figure 3.** ~~$I_{WR}$ for all seven weather regimes around the EuBL life cycle in March 2016.~~ Weather regime index ($I_{WR}$) for all seven weather regimes around the EuBL life cycle in March 2016 shown for the year-round weather regime definition from February 24, 00 UTC–March 27, 00 UTC for all seven Euro-Atlantic regimes: Atlantic Trough (AT), Zonal (ZO), Scandinavian Trough (ScTr), Atlantic Ridge (AR), European Blocking (EuBL), Scandinavian Blocking (ScBL) and Greenland Blocking (GL). Thick lines represent active regime life cycles. gray shading indicates the period of the active EuBL regime life cycle from March 9, 18 UTC–March 18, 00 UTC.

normalized projection of $q^L$ and its tendencies onto the low-frequency PV pattern of the weather regime, $q_{WR}^L$:

$$P_{q^L}(t) = \frac{\sum_{(\lambda,\varphi)} q^L(t,\lambda,\varphi) \, q_{WR}^L(\lambda,\varphi) \cos\varphi}{\sum_{(\lambda,\varphi)} q_{WR}^{L\,2}(\lambda,\varphi) \cos\varphi} \qquad \text{and} \qquad P_{\partial q^L/\partial t}(t) = \frac{\sum_{(\lambda,\varphi)} \partial q^L(t,\lambda,\varphi)/\partial t \, q_{WR}^L(\lambda,\varphi) \cos\varphi}{\sum_{(\lambda,\varphi)} q_{WR}^{L\,2}(\lambda,\varphi) \cos\varphi} \,. \tag{6}$$

Note ~~here, that the~~ that the projection of the tendency is equivalent to the tendency of the projection $P_{q^L}$ because $q_{WR}^L$ is constant with time and the operator $\partial/\partial t$ commutes with the summation operator. The normalized projection is performed over the northern hemisphere in the latitudinal band between 25 °N and 80 °N since the PV tendencies are limited to this domain. The low-pass filtered anomaly $q^L$ is averaged between 315 and 325 K (~~Sect.~~Section 2.2). The weather regime PV pattern $q_{WR}^L$ is defined as the mean of the low-frequency PVAs vertically averaged between 500 and 150 hPa on active life-cycle days (shown for EuBL in ~~Fig.~~Figure 2b), consistent with the definition used in the quasi-Lagrangian perspective to track PVAs (~~Sect.~~Section 2.5). Analogous to the definition of the $I_{WR}$ in ~~Sect.~~Section 2.3, we subtract the climatological background value and do a standardization. $P_{q^L}$ then closely resembles the $I_{WR}$ and describes how similar a certain PV pattern is to one of the weather regimes (~~Eq.~~Equation 5). The similarity of $P_{q^L}$ and $I_{WR}$ is shown for the EuBL regime life cycle in March 2016 in ~~Fig.~~Figure 4. Due to the large qualitative agreement, we conclude that the dynamics underlying the evolution of $I_{WR}$ can be interpreted in terms of the dynamics of $P_{q^L}$.

The individual contributions governing the evolution of $P_{q^L}$ (namely the quasi-barotropic term - QB, the baroclinic term - BC, the divergent term - DIV, the convergence of the eddy flux term - EDDY, non-conservative term - NON-CONS, and the residual term - RES) are obtained by applying our 10-day low-pass filter to each term in ~~Eq.~~Equation 4 and inserting that term
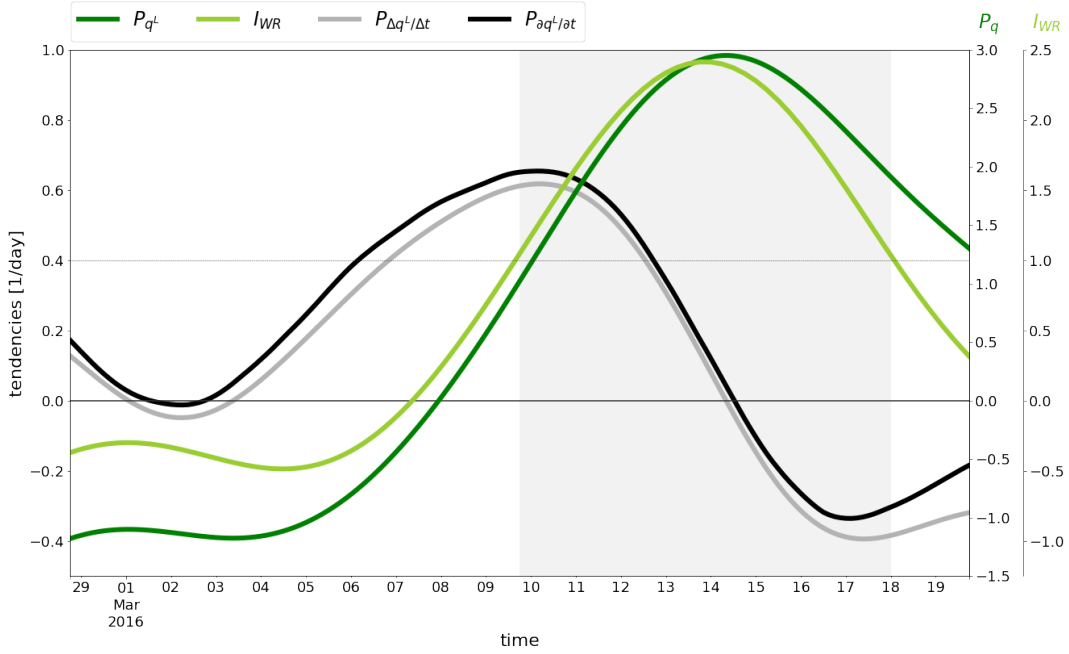
**Figure 4.** ~~Difference between the $I_{WR}$ evolution and the evolution of the projected low-frequency PVAs to the EuBl regime pattern $P_q$.~~ Difference between the $I_{WR}$ evolution and the evolution of the projected low-frequency PVAs to the EuBl regime pattern $P_q$. Projection of 10-day low-pass filtered PVAs ($P_q$, dark green) and $I_{WR}$ in terms of geopotential height anomalies at 500 hPa (light green, cf. Fig 3) on the right y-axes. The gray and black solid line represent the projection of the observed ($P_{\Delta q^L/\Delta t}$) and the diagnosed (DIAG = $\sum_j P_{\partial q^L/\partial t}\big|_j$) evolution of the PVAs, respectively (left y-axis). The gray shaded area denotes the ~~time span~~ period of the active life cycle defined by $I_{WR} \geq 1$.

into the RHS of ~~Eq.~~Equation 6.

$$P_{\partial q^L/\partial t}(t)\big|_j = \frac{\sum_{(\lambda,\varphi)\in NH} \frac{\partial q^L(t,\lambda,\varphi)}{\partial t}\big|_j q^L_{WR}(\lambda,\varphi)\cos\varphi}{\sum_{(\lambda,\varphi)\in NH} q^L_{WR}{}^2(\lambda,\varphi)\cos\varphi}, \qquad j \in \text{QB, BC, DIV, EDDY, NON-CONS, RES}.$$

255   This leads to the projection defined as

$$P_{\partial q^L/\partial t}(t)\big|_j = \frac{\sum_{(\lambda,\varphi)\in NH} \frac{\partial q^L(t,\lambda,\varphi)}{\partial t}\big|_j q^L_{WR}(\lambda,\varphi)\cos\varphi}{\sum_{(\lambda,\varphi)\in NH} q^L_{WR}{}^2(\lambda,\varphi)\cos\varphi}, \qquad j \in \text{QB, BC, DIV, EDDY, NON-CONS, RES}, \tag{7}$$

~~Technically, the projection~~ which describes a normalized pattern correlation between the low-frequency PV tendencies and the regime pattern. If a projection is positive, the associated process favors a given regime pattern. If a projection is negative, the associated process works against a regime pattern. The observed temporal evolution of $P_{q^L}$ agrees very well with the

260   diagnosed evolution, $\sum_j P_{\partial q^L/\partial t}\big|_j$ (~~Fig.~~Figure 4). There is a near-constant difference of $0.07\text{d}^{-1}$ between the diagnosed and

observed evolution (a relative difference of 12% at onset time), which increases during the decay stage of the regime. However, the diagnosed tendencies still capture the overall evolution of $P_{q^L}$ very well. In combination with the relative smallness of the difference we thus assert that the assessment of the relative importance of individual processes is not compromised.

## 2.5 Quasi-Lagrangian perspective on the amplitude evolution of negative PVAs contributing to a weather regime

265 We complement the Eulerian perspective with a quasi-Lagrangian perspective that follows upper-tropospheric anticyclonic PVAs in blocked weather regime life cycles and quantifies the processes in their PVA amplitude evolution. To identify contributing PVAs we ~~(i)~~ first identify and track negative upper-tropospheric PVAs as the vertical average between 500 and 150 hPa based on ERA5 model level data ~~, and (ii)~~ and then define the spatial overlap of each of the identified PVAs with the defining weather regime PV pattern. The identification and tracking of negative PVAs closely ~~follows~~ follow the blocking diagnostics

270 of Schwierz et al. (2004), with the following modifications: (i) PVAs are calculated as deviations from a 30-day running mean climatology (~~1979–2019) centered at~~ 1980–2019) centered on the respective calendar ~~time~~ day, (ii) PVAs are not smoothed in time but smoothed spatially over a scale of 150 km, (iii) a weaker threshold of -0.8 PVU is used ~~to identify PVAs earlier and to increase their spatial extent, respectively,~~ which enables early detection, and (iv) the spatial overlap criterion for the tracking of the PVAs is reduced to a minimum (overlap > 0 %) to enable the tracking of ~~fast moving~~ fast-moving, transient PVAs (as

275 compared to quasi-stationary PVAs in Schwierz et al. (2004)). The ~~fix~~ fixed threshold of -0.8 PVU is used exclusively in this case study and captures approximately the 35 % strongest negative PVAs in the northern hemisphere in terms of area for the period ~~1979-2019. Even if the chosen threshold does not cover the entire anomaly area, we see the clear advantage here that individual dynamic anomalies are not grouped together in a single large anomaly.~~

1980–2019. In this context, the threshold value fulfills both conditions required: (1) It is close enough to $q' = 0$ such that

280 the budget of the integrated PVA amplitude of Teubler and Riemer (2016) can be closed as good as possible, and (2) it is far enough away from $q' = 0$ such that the grouping of PVAs over the entire northern hemisphere by single thin filaments is avoided, which enables the investigation of single distinct PVAs. Furthermore, the algorithm is modified to identify splitting and merging events. For further details about the identification and tracking the interested reader is referred to the appendix (~~Sect.~~ Section A, ~~Fig.~~ Figure A1). In the remainder of this study, the negative upper-tropospheric PVAs identified and tracked in

285 the quasi-Lagrangian perspective are referred to PVAs$_{qL}^{-}$ in the following.

The assignment of PVAs$_{qL}^{-}$ to active weather regime life cycles is based on the spatial overlap with a predefined regime mask. The regime mask is defined as the area encapsulated by the area where the values of the weather regime pattern are smaller than $-0.3$ PVU (bright green contour line in ~~Fig.~~ Figure 2b). PVAs$_{qL}^{-}$ that exhibit at least 10 % overlap with the regime mask at the time of an active regime are attributed to that specific regime life cycle. In general, more than one PVA$_{qL}^{-}$ may

290 contribute to a given regime life cycle.

We apply the PV framework of Teubler and Riemer (2016) to PVA$_{qL}^{-}$ tracks and consider the importance of processes that contribute to the amplitude evolution. This ~~gives us~~ allows for deeper insights into the associated dynamics. Our amplitude metric is the spatial integral of $q'$ over the area $A$ of the PVA$_{qL}^{-}$, i.e., $\int_{\mathcal{A}} q' dA$. ~~The~~ Using the Leibniz integral rule, the

295   tendency equation for this amplitude metric ~~follows Teubler and Riemer (2021, their Eq. 6). Note that the identification and tracking of $\mathrm{PVA}_{qL}^{-}$ is performed on pressure levels, whereas the PV framework of Teubler and Riemer (2021) is based on isentropic levels. We hence define the area $\mathcal{A}$ by the overlap of $\mathrm{PVA}_{qL}^{-}$ with the negative PVA at the respective isentropic levels. Teubler and Riemer (2016) considered anomalies that were bounded, in general, by $q' = 0$ on the respective isentropic level, which is not the case in the present study.~~

300   ~~The presentation here thus deviates in the discussion of the boundary term $Bnd$. Furthermore, we use a somewhat different definition of the residuum $RES$. For the sake of consistency with the Eulerian perspective above, we make an inconsequential further modification: the (very small) term $\boldsymbol{v}_0 \cdot \boldsymbol{\nabla} q_0$ is attributed to $RES$ here instead of Teubler and Riemer's quasi-barotropic term.~~

  ~~Using the Leibniz integral rule, we obtain~~

305
$$\frac{d}{dt} \int_{\mathcal{A}} q' \, dA = \int_{\mathcal{A}} \frac{\partial q'}{\partial t} \, dA + \oint_{\mathcal{S}} q' \boldsymbol{v}_s \cdot \boldsymbol{n} \, dS,$$

~~with the~~ following Teubler and Riemer (2021, their Equation 6) is given by

$$\frac{d}{dt} \int_{\mathcal{A}} q' \, dA = \int_{\mathcal{A}} \frac{\partial q'}{\partial t} \, dA + \oint_{\mathcal{S}} q' (\boldsymbol{v}_s \cdot \boldsymbol{n}) \, dS, \tag{8}$$

with the normal vector $\boldsymbol{n}$ in outward direction of the boundary $\mathcal{S}$ of $\mathcal{A}$ and $\boldsymbol{v}_s$ is the motion of $\mathcal{S}$. The first term on the right describes the contributions to the amplitude strength whereas the second term represents the contribution to the area change.

310   We expand the first term ~~on~~ of the RHS according to the partitioning introduced in ~~Eq.~~ Equation 4, ~~moving termsthat merely redistribute existing PVAs to $Bnd$:~~

$$\frac{d}{dt} \int_{\mathcal{A}} q' \, dA = -\int_{\mathcal{A}} \boldsymbol{v}_{up} \cdot \boldsymbol{\nabla} q_0 \, dA - \int_{\mathcal{A}} \boldsymbol{v}_{bc} \cdot \boldsymbol{\nabla} q_0 \, dA + \int_{\mathcal{A}} [q' (\boldsymbol{\nabla} \cdot \boldsymbol{v}_{div}) - \boldsymbol{v}_{div} \cdot \boldsymbol{\nabla} q_0] \, dA + \int_{\mathcal{A}} \mathcal{N} \, dA + Bnd + RES,$$

~~with~~

$$RES := \int_{\mathcal{A}} \left[ (\boldsymbol{v}_{res} + \boldsymbol{v}_0) \cdot \boldsymbol{\nabla} q_0 + q'(\boldsymbol{\nabla} \cdot \boldsymbol{v}_{res}) + \frac{\partial q_0}{\partial t} \right] dA$$

315   ~~and (using the Gauss theorem)~~

$$Bnd := \oint_{\mathcal{S}} q' (\boldsymbol{v}_s - \boldsymbol{v}) \cdot \boldsymbol{n} \, dS = \int_{\mathcal{A}} \boldsymbol{\nabla} \cdot (q'(\boldsymbol{v}_s - \boldsymbol{v})) \, dA.$$

~~Note that the~~ 3 which yields

$$\frac{d}{dt} \int_{\mathcal{A}} q' \, dA = \underbrace{\int_{\mathcal{A}} -\boldsymbol{v}'_{up} \cdot \boldsymbol{\nabla} q_0 \, dA}_{QB} + \underbrace{\int_{\mathcal{A}} -\boldsymbol{v}'_{low} \cdot \boldsymbol{\nabla} q_0 \, dA}_{BC} + \underbrace{\int_{\mathcal{A}} [-\boldsymbol{v}'_{div} \cdot \boldsymbol{\nabla} q_0 + q'(\boldsymbol{\nabla} \cdot \boldsymbol{v}'_{div})] \, dA}_{DIV} + \underbrace{\int_{\mathcal{A}} \mathcal{N} \, dA}_{NON-CONS} + \underbrace{\int_{\mathcal{A}} -\boldsymbol{v}_0 \cdot \boldsymbol{\nabla} q_0 \, dA}_{BGA} + \int_{\mathcal{A}} -\boldsymbol{v} \tag{9}$$

where we have rearranged terms, used the nondivergence of the balanced flow $(\boldsymbol{v}_0, \boldsymbol{v}'_{up}, \boldsymbol{v}'_{low})$ and assumed the residual wind $\boldsymbol{v}'_{res}$ to be nondivergent too[1]. The abbreviations, that are introduced in Equation 9 to denote the different PV tendency terms, appear in the figures in the quasi-Lagrangian perspective (Section 4.2 and are used for an easier reference. The (very small) term $\boldsymbol{v}_0 \cdot \nabla q_0$ is not attributed to Teubler and Riemer (2021)'s quasi-barotropic term for the sake of consistency with the Eulerian perspective above. The major contribution to the amplitude change of the anomaly (~~Eq.~~Equation ~~??~~9) is due to terms of the form ~~$\boldsymbol{v} \cdot q_0$, i.e., due to terms~~ $\boldsymbol{v} \cdot \nabla q_0$ that describe that air masses cross the gradient of background PV.

The ~~term $RES$ is generally small (see Sect. B, Fig. B1)~~ boundary term $BND$ is introduced that describes the change in the integration area $\mathcal{A}$ by (i) the net divergence of the PVA flux $(-\boldsymbol{v}q')$ through the boundary, and by (ii) the movement of the boundary $\boldsymbol{v}_s$. Note that the eddy term in ~~Eq.~~Equation 4 is completely absorbed into ~~Bnd. The definition of $Bnd$ is motivated by the fact that the term vanishes if~~ the first term of $BND$ (Equation 9. Teubler and Riemer (2016) considered anomalies that were bounded, in general, by $q' = 0$ ~~along the boundary $\mathcal{S}$~~ on the respective isentropic level. In this case, $BND$ is sufficiently small so that it can be neglected. In this study, the identification and tracking of $\mathrm{PVA}^-_{qL}$ is performed on pressure levels. We hence define the integration area $\mathcal{A}$ by the overlap of $\mathrm{PVA}^-_{qL}$ with the negative PVA on isentropic levels (315, 320, and 325 K). As a consequence, $BND$ no longer cancels out during integration. Generally, $BND$ is difficult to determine since the motion of the boundary of the anomaly $\boldsymbol{v}_s$ is required. Section B in the appendix discusses inherent limitations to the evaluation of ~~$Bnd$. Evaluating $Bnd$~~ $BND$. Evaluating $BND$ by using observed changes $\Delta A$ of the area $A$ of the PVA on isentropic levels, we find a very good agreement between the observed and the diagnosed tendency of the amplitude (~~Fig.~~Figure B1~~).~~ a).

In the following, we will in particular focus on the first four terms in ~~Eq.~~Equation ~~??,~~ 9 (QB, BC, DIV, and NON-CONS), i.e., on those that yield amplitude changes in the globally-integrated sense. This focus implies the assumption that the relative importance of the processes diagnosed *within* the $\mathrm{PVA}^-_{qL}$ – defined by a finite threshold – is similar to that *in the vicinity* of the $\mathrm{PVA}^-_{qL}$. *Vicinity* is here defined as the area between the contour line of the finite $q'$ threshold and a neighboring $q' = 0$ contour line. ~~It is from this vicinity that anomalies may be redistributed to within the $\mathrm{PVA}^-_{qL}$. From the quasi-Lagrangian perspective, in contrast to the Eulerian perspective, we thus do not consider fluxes of $q'$ as a process of interest in its own right~~However, for completeness, the temporal evolution of the terms contained in the second row of Equation 9 are presented in the appendix (Figure B1).

---

[1] Nonlinearly balanced flow is nondivergent and we consider the residual wind to largely stem from the decomposition of the nondivergent flow by piecewise PV inversion. We find, however, that the individual balanced flow components exhibit small but non-negligible values of horizontal divergence when evaluating on isentropic levels. We attribute this spurious divergence to numerical inaccuracies when interpolating from pressure to isentropic levels and the simplification of using the horizontal wind only for the interpolation and when evaluating divergence. For the sum of $\boldsymbol{v}_0 + \boldsymbol{v}'_{up} + \boldsymbol{v}'_{low} + \boldsymbol{v}'_{res}$, however, the divergence vanishes. Therefore, we now do not further consider the spurious individual terms in our PV budget.

## 2.6 Lagrangian perspective on the diabatic history of air parcels ending up in the $PVA^-_{qL}$

We complement the Eulerian and quasi-Lagrangian perspectives by a Lagrangian perspective that focuses on the diabatic history of air parcels that end up in the $PVA^-_{qL}$ associated with a blocked regime. We employ the Lagrangian analysis tool LAGRANTO (Sprenger and Wernli, 2015), using three-dimensional wind fields from ERA5 model level data. The diabatic history of air parcels is investigated with a set of three-day backward trajectories that end up in the $PVA^-_{qL}$ defined in the quasi-Lagrangian perspective (~~Seet~~Section. 2.5). Following Pfahl et al. (2015), trajectory calculations are launched for each grid point within a $PVA^-_{qL}$ ($\Delta$x = 0.5 °) on nine pressure levels between 500 and 150 hPa ($\Delta$ p = 50 hPa) for each time step. In accordance with Pfahl et al. (2015) and Steinfeld and Pfahl (2019), we trace potential temperature $\theta$ along the trajectories, and the three-day backward trajectories are classified based on their net change of $\theta$ along the trajectory. Trajectories are classified as diabatically 'heated' if $\Delta\theta_{h,max} > 2\,\mathrm{K}$ is fulfilled.

In addition, we create an additional set of trajectories to detect WCBs as trajectories that ascend by at least 600 hPa in 48 hours based on a similar methodology as Madonna et al. (2014). Analogous to Quinting and Grams (2022), we distinguish different stages of the WCB and assign all WCB trajectory parcels that are located above 400 hPa to the WCB outflow stage. For this purpose, two-day backward trajectories are started 3-hourly in the northern hemisphere at an equidistant grid of $\Delta x$ = 100 km and at 13 equidistant vertical levels between 400 and 100 hPa. This is not the traditional way to determine WCB outflow by forward trajectories ~~,~~but offers the advantage of calculating trajectories directly from the $PVAs^-_{qL}$. The filtering of trajectories is omitted here to avoid double counting as well as the criterion that the ascent must take place in the vicinity of an extratropical cyclone.

## 3 PV evolution of the EuBL regime life cycle in March 2016

This section introduces the synoptic and large-scale evolution of the EuBL weather regime life cycle in March 2016. Based on the IWR, the life cycle occurred from March 9, 18 UTC to March 18, 00 UTC (~~Fig.~~Figure 5). We first discuss the PV-based evolution of the large-scale flow features in the North Atlantic-European region. This is complemented by a first overview of the potential influence of moist processes in the development of the blocked regime pattern, based on divergent PV tendencies and WCB intersection points with the 320 K isentropic surface in the upper troposphere.

The large-scale circulation pattern is characterized by a high-amplitude ridge over the North Atlantic five days prior to regime onset (black 2-PVU contour and strong negative PVA in blue shading, ~~Fig.~~Figure 5a). This ridge is flanked by broad troughs upstream over eastern North America and downstream over western Europe (positive PVAs in gray shading). An incipient negative upper-tropospheric PVA develops at the southern flank of the trough upstream near the U.S. East Coast (light green contour in ~~Fig.~~Figure 5a). This negative PV anomaly is later in this study identified as the main contributing $PVA^-_{qL}$ from a quasi-Lagrangian perspective. The broad trough over western Europe occupies the region where a quasi-stationary ridge is expected later during the EuBL life cycle (see thin dashed lines in black, ~~Fig.~~Figure 5a). Over the next four days, the incipient ridge over the North Atlantic dramatically amplifies ahead of a narrowed and elongated trough along the U.S. East Coast and
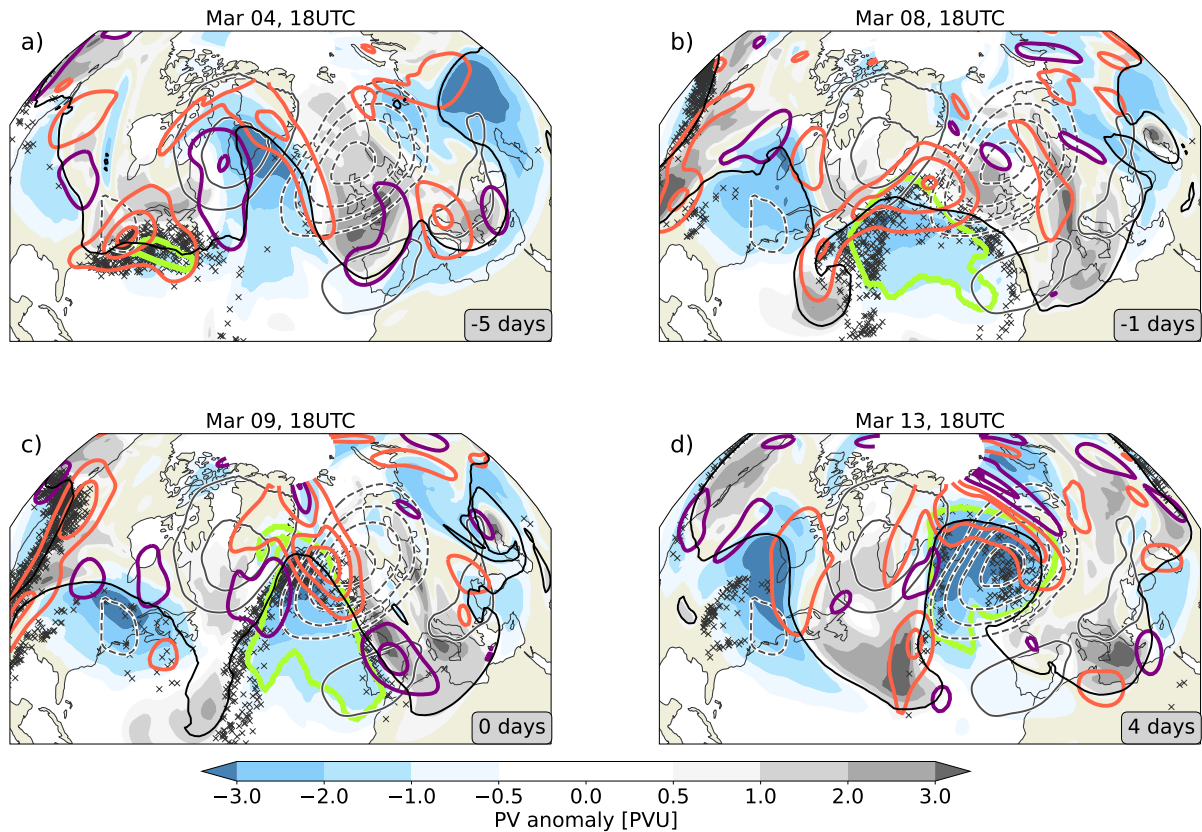
**Figure 5.** ~~Synoptic evolution of the EuBL regime life cycle in March 2016.~~ Synoptic evolution of the EuBL regime life cycle in March 2016. Upper-tropospheric PVAs (315–325 K isentropic layer mean, shading) and the 2-PVU contour (solid black) for selected time lags relative to the EuBL regime life cycle onset (March 9, 18 UTC): (a) five days ~~prior to~~ before onset, (b) the day ~~prior to~~ before onset, (c) onset, and (d) four days after onset. The negative PV anomaly that is later identified in the quasi-Lagrangian perspective in ~~Sect.~~Section 4.2 ($PVA_{qL}^{-}$) as the main contributing negative PVA is shown in a light green contour line (corresponds to the -0.8 PVU anomaly contour). ~~Red~~ Orange and ~~dark~~ purple solid contour lines point to negative and positive divergent PV tendencies ($-\boldsymbol{v}_{div} \cdot \boldsymbol{\nabla} q - \boldsymbol{v}_{div}' \cdot \boldsymbol{\nabla} q$) likewise shown as the isentropic mean between 315–325K (in steps of +/- 0.5, 1.5, 2.5 PVU day$^{-1}$). Note that divergent PV tendencies are smoothed by a Gaussian filter. Black crosses mark every ~~fifth~~ thirty intersection point of WCB trajectories in the 317.5–322.5 K isentropic layer. The thin dark grey contours indicate the regime pattern of EuBL ($\pm$ (0.2, 0.4, 0.6, 0.8) PVU, negative dashed).

extends to the east where it replaces the high-amplitude ridge over the North Atlantic (Fig 5b). During the same period, the large-amplitude trough downstream has slowly moved from western to central Europe (Fig 5a,b). Around one day prior to the EuBL onset, the trough upstream reaches far to the south, exhibits a cut-off character, and wraps up cyclonically. One day later at the time of the EuBL onset, the ridge is centered over the eastern North Atlantic upstream of the region of the climato-

385 logical mean negative PVA during EuBL (~~Fig.~~Figure 5c). The troughs upstream and downstream of the ridge also ~~increase in amplitude (measured in PVA)~~strengthen as manifested by the increasing PV anomaly magnitude within these areas. A further

intensification of the negative PVA occurs during the 4 days of the active regime life cycle resulting in a highly amplified ridge at the time of the maximum manifestation of the blocked regime (defined as maximum in $I_{WR}$ in ~~Fig.~~ Figure 3). At that time, the ridge covers a large area over the eastern North Atlantic and northwestern Europe and starts breaking anticyclonically
390 towards central Europe (~~Fig.~~ Figure 5d). The trough downstream is displaced to the southeast and has weakened, but the trough upstream continues to strengthen and still reaches far to the south.

~~In order to~~ To understand the impact of moist processes for the development and maintenance of the EuBL regime life cycle, we look at divergent PV tendencies and WCB air parcels at 320 K. High WCB activity prevails over the U.S. East Coast at the
395 time when the incipient negative PVA develops and suggests a moist contribution to the formation of the PVA (~~Fig.~~ Figure 5a). Simultaneously, divergent PV tendencies centered at the northwestern corner of the anomaly strengthen the negative PVA (red contours). On the day before the EuBL onset, again strong negative divergent PV tendencies co-occur with WCB air parcels, especially on the northwestern flank of the ridge associated with the upstream trough (~~Fig.~~ Figure 5b). Studies by Magnusson (2017) and Grams et al. (2018) have shown that synoptic-scale WCB activity associated with this upper-level trough con-
400 tributed to the subsequent amplification and poleward extension of the ridge. This has further been demonstrated to largely amplify forecast errors, leading to a particularly poor medium-range forecast over Europe. At the time of the regime onset, high WCB activity is observed on the eastern and western flanks of the large-amplitude ridge around the EuBL onset, with a clear center of action located at the northern tip (~~Fig.~~ Figure 5c). Here we see again that this is accompanied by strong divergent PV tendencies that are associated with an amplification of the ridge. At the same time, positive divergent PV tendencies are
405 now appearing on the flanks of the ridge indicating a narrowing. During the life cycle, it becomes clear that the maintenance of the regime involves a diabatic contribution implied by strong negative divergent PV tendencies in the northern corner of the ridge (~~Fig.~~ Figure 5d). Ongoing WCB activity is observed ahead of the high-amplitude cyclonically-breaking trough upstream.

In summary, the development and maintenance of the EuBL life cycle in March 2016 ~~is~~ are related to the propagation
410 and amplification of a negative PVA reaching Europe around the time of regime onset. The amplification of this negative PVA and its maintenance over Europe is associated with intermittent synoptic activity that points to a non-negligible moist-dynamical contribution. A fair agreement is seen in the spatial occurrence of WCB air parcels and ridge-amplifying divergent PV tendencies ~~,~~ so that the consideration of the divergent PV tendency term as an indirectly diabatic term is justified. It is important to note that the negative PVA is not generated locally over Europe, but quite far upstream. Likewise, the synoptic
415 activity, which seems to be an important contributor in the buildup of the regime, takes place upstream of where the block is expected. In the following, we will quantify the contributions of different processes to the EuBL regime life cycles from the Eulerian, quasi-Lagrangian ~~and Lagrangian perspective~~, and Lagrangian perspectives.

# 4 Three perspectives on the PV dynamics of the EuBL regime life cycle in March 2016

## 4.1 Eulerian PV perspective

We consider the onset, maintenance, and decay of the EuBL regime over the North Atlantic-European region from the Eulerian perspective by focusing on the processes that locally contribute to a certain regime pattern. Low-pass filtered PV tendencies are projected onto the regime pattern to quantitatively determine the mechanisms that govern the evolution of the regime pattern. Further insight into the dynamics of the pattern evolution can be gained by considering the positive and negative PVAs separately, i.e., by projecting the individual tendencies only onto the positive (trough) and negative (ridge) parts of the pattern, respectively. The individual contributions of different processes to the evolution of the EuBL regime pattern are shown as tendencies in Figure 6. Positive values indicate that an individual mechanism contributes to the onset of the regime pattern and negative values imply that a particular process contributes to the decay of the regime pattern. The time series of the tendencies is complemented with spatial information on PV and PV tendencies for selected times in Figure 7.

The most dominant contribution to the regime pattern evolution around the onset arises from linear wave dynamics as described by the quasi-barotropic PV tendency (Figure 6a). As discussed in Section 2.2, this PV tendency term describes the residual of the (westward) intrinsic phase propagation and the eastward advection of PVAs by the background flow. During the considered period, the latter term dominates, and thus the downstream advection of PVAs is of crucial importance for the onset of the regime pattern. We have already shown in Section 3 that the negative PVA ($\mathrm{PVA}^-_{qL}$), which later represents the block over Europe, forms upstream. Considering negative and positive PVAs separately, the propagation of this $\mathrm{PVA}^-_{qL}$ from upstream to the target region is reflected in large values of the quasi-barotropic tendency in the projection (Figure 6c) and amplifying quasi-barotropic tendencies in the ridge of the regime pattern (Figure 7d,f). A consistently positive contribution from the quasi-barotropic term for the cyclonic part of the regime pattern underlines the propagation of positive PVAs, but the contribution is much smaller (Figure 6b, Figure 7d,f). Baroclinic PV tendencies are predominantly associated with the maintenance of the regime pattern but do not play a leading role in its onset (Figure 6a). However, they become important in counteracting other PV tendency terms towards the end of the life cycle. The contributions to the full regime pattern arise predominantly from the anticyclonic part of the regime pattern, suggesting a contribution to the amplification of the ridge over Europe (Figure 6c). However, a closer look at the spatial pattern reveals that the baroclinic term contributes to the secondary anticyclonic part of the regime pattern located over the U.S. East Coast and not to that related to the block itself (Figure 7f,h). The divergent PV tendencies are of further importance in the onset stage of the EuBL regime pattern and show their maximum positive contribution to the onset of the pattern around March 9, 18 UTC (Figure 6a). Divided into the anticyclonic and cyclonic parts of the regime pattern, the divergent term almost exclusively contributes to the former and weakens the latter with a large contribution to the regime decay in the second half of the regime life cycle (Figure 6b,c; Figure 7c,e,g). Negative divergent PV tendencies overlap with the cyclonic regime pattern over the central North Atlantic at that time (Figure 7g), which could be related to the onset of the subsequently established Atlantic Ridge regime pattern (Figure 3).
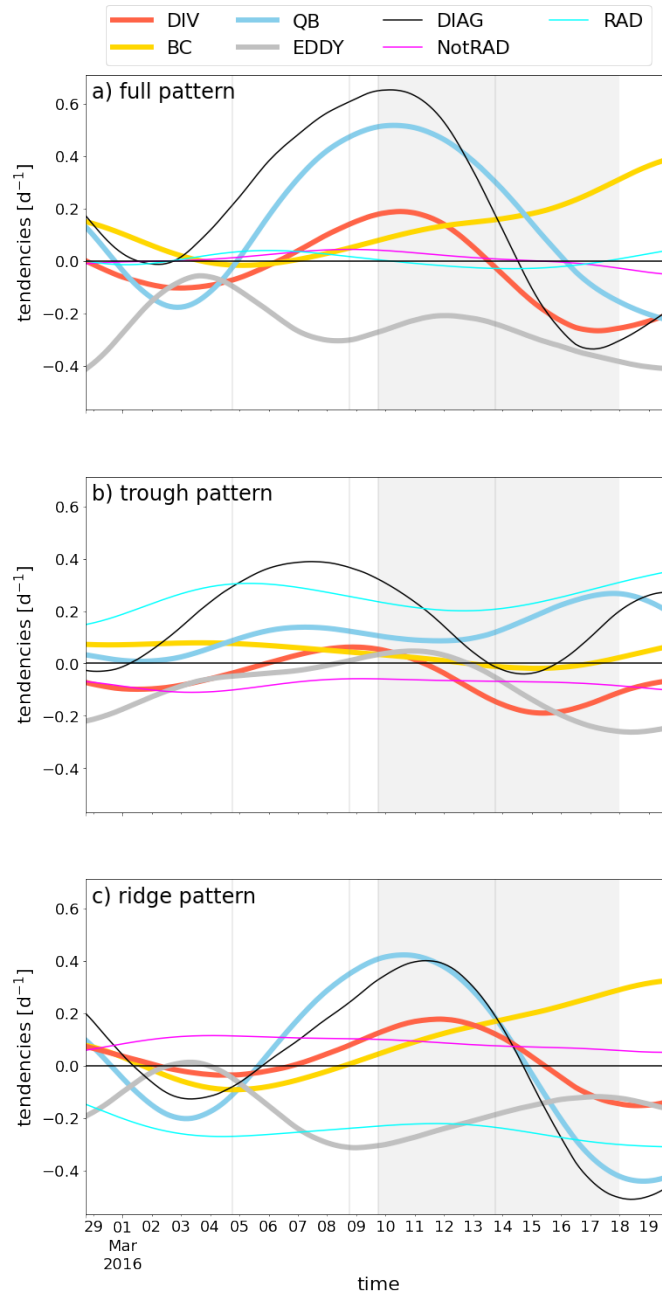
**Figure 6.** ~~Quantified PV dynamics of the EuBL regime life cycle in March 2016 from a Eulerian perspective.~~ Quantified PV dynamics of the EuBL regime life cycle in March 2016 from an Eulerian perspective. Projection of low-frequency PV-tendencies (in day$^{-1}$) onto (a) the full regime pattern consisting of positive and negative PVAs, (b) only the positive PVAs, and (c) only the negative PVAs of the regime pattern. The colored curves represent the different PV tendencies: divergent (DIV, red), quasi-barotropic (QB, blue), baroclinic (BC, yellow), and the convergence of eddy fluxes (EDDY, gray). The contribution due to direct diabatic modification is separated into radiation (RAD, turquoise) and non-radiative processes (NotRAD, pink). The full diagnosed tendency (DIAG) is displayed as the sum of all the terms included in Equation 7 (black curve). The gray shaded area denotes the time of the active EuBL regime life cycle. Gray vertical lines refer to the times for which spatial fields of PVAs and PV tendencies are shown in ~~Fig.~~ Figure 7.
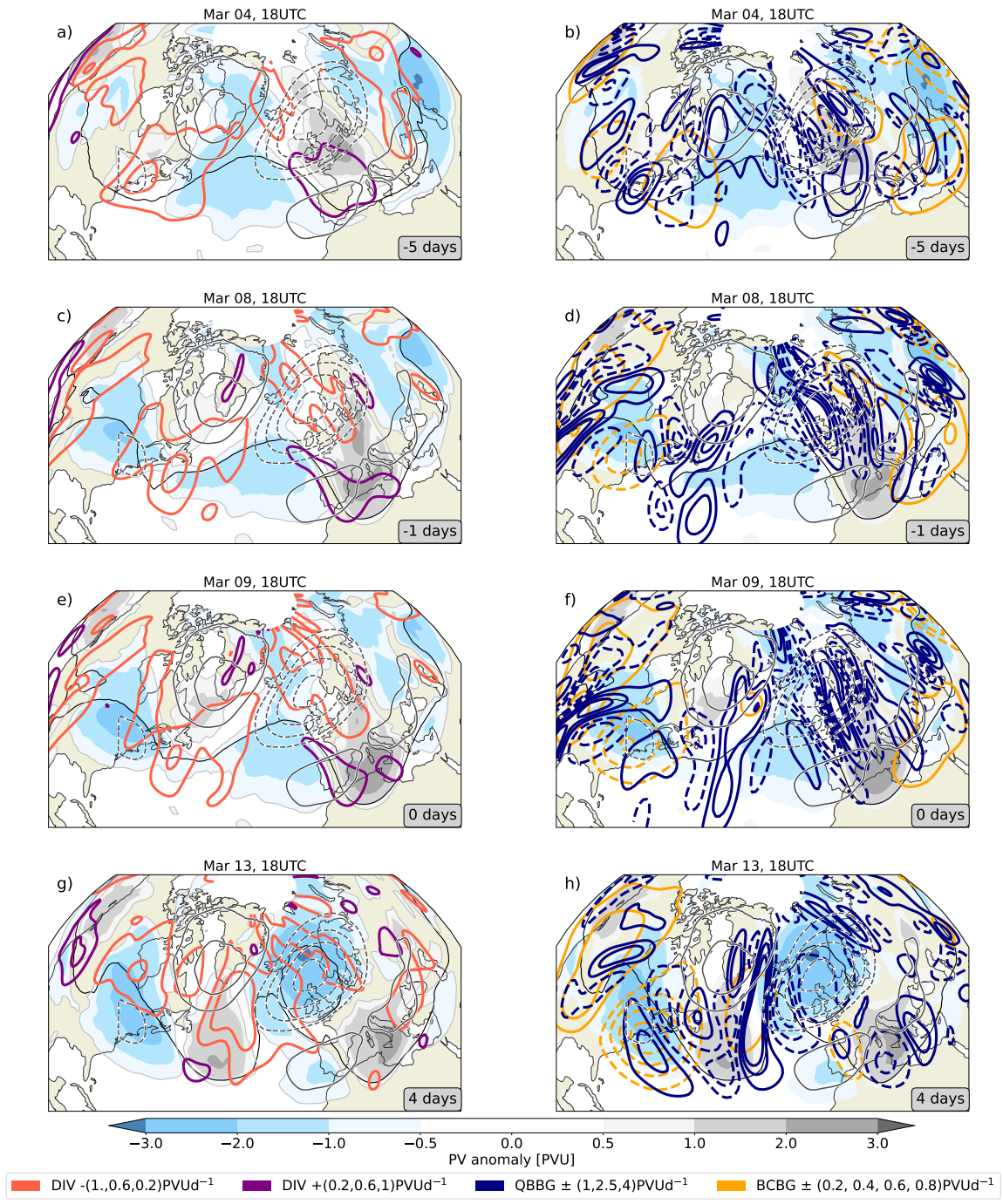
**Figure 7.** ~~Snapshots of the low-frequency PV evolution around the EuBL regime life cycle.~~ Snapshots of the low-frequency PV evolution around the EuBL regime life cycle. Low-frequency PVAs (315–325 K averages) are shown in shading (in PVU), the 2-PVU contour is shown as thick black line, and the thin dark grey lines show the EuBL regime pattern used to project the PV tendencies and PVAs into (dashed for negative and solid for positive). Divergent PV tendencies are smoothed by a Gaussian filter and shown in contour lines in the left column (see lower left colorbar). Blue contour lines point to quasi-barotropic PV tendencies and yellow contour lines to baroclinic PV tendencies in the right column (see colorbar in the lower right). For the quasi-barotropic and baroclinic tendencies, solid (dashed) contour lines display positive (negative) PV tendencies. The snapshots are shown for five days ~~prior to~~ before onset (panels a,b), the day ~~prior to~~ before onset (panels c,d), onset (panels e,f), and four days after onset (panels g,h). The selected time steps are marked as vertical grey lines in the projection timeline in ~~Fig.~~ Figure 6.

Nonlinear processes as diagnosed by the convergence of non-divergent eddy fluxes have been ~~in~~ the focus of many previous studies. In this case, they are negative, such that they neither support the onset nor the maintenance of the pattern in the current case and are consistently associated with the decay of the regime pattern (~~Fig.~~Figure 6a). A clear minimum is visible in the
455    separate consideration of the anticyclonic part of the pattern around the onset, where nonlinear processes such as wave breaking are associated with a decay of the regime pattern (~~Fig.~~Figure 6c). Note, however, that the eddy fluxes may still help to maintain the regime pattern by reducing the strength of the westerly flow upstream (Illari, 1984). A dipole pattern associated with the eddy fluxes that indicates such a reduction is found in the average over many cases of Greenland blocking (Teubler et al., 2022).

460    When the two diabatic PV tendency terms - radiative and non-radiative tendencies - are considered together, their effect on the regime onset and decay cancel out almost completely (~~Fig.~~Figure 6a). The radiative tendency strengthens the cyclonic part of the regime pattern and weakens the anticyclonic part (~~Fig.~~Figure 6b,c). Thereby, the projected tendency is almost constant and changes only slowly indicating that the radiative diabatic tendency is not closely linked to the mechanisms governing the regime evolution. While non-radiative diabatic tendencies are associated with a decay of the cyclonic regime part, they
465    strengthen the anticyclonic part of the regime suggesting that these tendencies are dominated by latent heat release.

The Eulerian perspective elaborates on the importance of the advection of existing PVAs by the background flow in the onset stage of the EuBL regime pattern. From this perspective, divergent PV tendencies have a non-negligible effect in building up the anticyclonic part of the regime. However, the Eulerian perspective misses the processes associated with the development
470    of PVAs advected into the region. Further insights ~~in~~ into the evolution of these PVAs can be gained by tracing the PVAs that are advected into the region, especially the negative PVAs associated with the anticyclonic part of the pattern over Northern Europe ($PVAs_{qL}^-$).

## 4.2   Quasi-Lagrangian PV perspective

The quasi-Lagrangian perspective focuses on traced anticyclonic PVAs in the Northern Hemisphere ($PVAs_{qL}^-$) that contribute
475    to a blocked regime life cycle and their amplitude evolution. In contrast to the low-frequency Eulerian perspective above, here
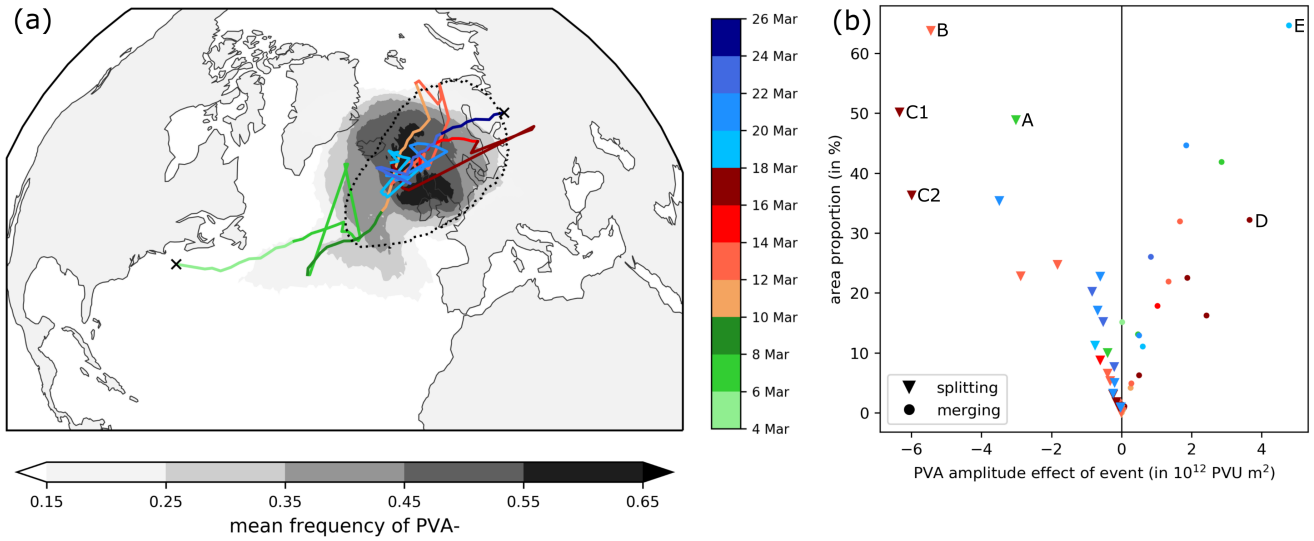
**Figure 8.** ~~Track of the PVA$_{qL}^-$ that contributed to the EuBL in March 2016 and detected splitting and merging events along the tracks.~~ Track of the PVA$_{qL}^-$ that contributed to the EuBL in March 2016 and detected splitting and merging events along the tracks. (a) The colored line shows the track of the PVA$_{qL}^-$ based on the center of mass from March 4, 15 UTC – March 25, 00 UTC. The time information is given in color shades (green: before regime onset, red: active regime life cycle, blue: after regime decay). Jumps in the PVA$_{qL}^-$ track can be attributed to abrupt changes in the center of mass due to splitting and merging events. The mean frequency of the PVA$_{qL}^-$ during the time of the track ( = percentage of the PVA$_{qL}^-$ lifetime on which the PVA$_{qL}^-$ overlaps a grid point) is shown in gray shading (in %). The black dotted contour highlights the regime mask of EuBL (same as in ~~Fig.~~Figure 2b). (b) Scatter plot that shows the association between the PVA$_{qL}^-$ amplitude effect of a splitting (triangle) or a merging (dot) event (in $10^{12}$ PVU m$^2$) and the area proportion of the splitting/merging PVA$_{qL}^-$ and the main PVA$_{qL}^-$ (in %). Each marker (triangle, dot) represents a splitting or merging event and the marker color indicates the time of the event. Particular events mentioned in the text are labeled with capital letters (and numbers).

we consider the instantaneous PV evolution. We will first discuss the track of the main PVA$_{qL}^-$ (already indicated in light green contours in ~~Fig.~~Figure 5) based on the center of mass coordinates, and splitting and merging events~~, then~~. Subsequently, we quantify the individual contributions to the amplitude evolution of the main PVA$_{qL}^-$, consider direct diabatic impacts separately, and finally conclude with a ~~brief~~ summary.

### Anomaly track and splitting and merging events

480

~~The~~ From a quasi-Lagrangian perspective, the EuBL life cycle in March 2016 was dominated by a single PVA$_{qL}^-$, which we identified from March 4–26. The PVA$_{qL}^-$ was first identified over the U.S. East Coast five days ~~prior to the~~ before regime onset and propagated northeastwards (~~Fig.~~Figure 8a). With the start of the EuBL life cycle on March 9, the PVA$_{qL}^-$ settled into a quasi-stationary position over northern Europe (illustrated by the ~~frequency maximum in Fig.~~maximum in frequency, Figure 8a). At the time of the regime decay, the PVA$_{qL}^-$ started to migrate further to the northeast. The end of the anomaly's

485

life cycle was reached seven days after the regime decay.

Abrupt changes in the track of the main $PVA_{qL}^-$ are evident in ~~Fig.~~Figure 8a, which are mainly due to splitting and merging events. These events cause sudden changes of the $PVA_{qL}^-$ amplitude and area, which in turn may prominently impact the position of the anomaly's center of mass. Our novel tracking algorithm in the quasi-Lagrangian perspective (~~Sect.~~Section 2.5, ~~Fig.~~Figure A1) is designed to detect and quantify the effect of these events. An overview of all splitting and merging events is provided in ~~Fig.~~Figure 8b. For approximately half of the events the impact on the $PVA_{qL}^-$'s area is relatively small (relative area change < 15 %) and, accordingly, that on area-integrated amplitude and ~~on~~ the main $PVA_{qL}^-$'s track. Other events, however, are accompanied by a significant change in area and amplitude and lead to jumps in the $PVA_{qL}^-$ track. For example, the prominent southward jump in the track around March 7 can be attributed to a splitting event, in which the northern part of the $PVA_{qL}^-$ area (that makes up approximately 50 % of the $PVA_{qL}^-$ ) splits off (~~Fig.~~Figure 8a,b; light green triangle with label 'A') and propagates towards the north (not shown). Another example is the merging event on March 19 (Figure 8b; light blue dot with label 'E') when a negative PVA of remarkable size (> 60 % of the $PVA_{qL}^-$ area) fed into the existing $PVA_{qL}^-$.

The majority of the anomalies that merge into the main $PVA_{qL}^-$ originates (up to three days prior to the merging event) from upstream and migrates into the main $PVA_{qL}^-$ from the southwest (~~Fig.~~Figure 9a). In contrast, the anomalies that split from the main $PVA_{qL}^-$ tend to move to the east of the main anomaly downstream into northern Asia (~~Fig.~~Figure 9b). Overall, splitting and merging events can have a substantial impact on the $PVA_{qL}^-$ amplitude evolution. For the first time, we can quantify this impact and compare the role of these events with other processes that impact the amplitude evolution~~(see discussion of Fig. 11 below).~~

**Amplitude evolution**

To quantify the processes that govern the amplitude evolution of ~~the main~~ $PVA_{qL}^-$, ~~Eq.~~Equation ~~?? is evaluated . As discussed in Sect. 2.5, we~~ 9 is evaluated on isentropic levels. Following Teubler and Riemer (2016, 2021), we will particularly focus on the ~~processes that lead to amplitude changes in a globally integrated sense and evaluate on isentropic levels,~~ four PV tendency terms on the first row in Equation 9 when we discuss the temporal evolution in the following. However, for the sake of completeness, the temporal evolution of the remaining terms in Equation 9 (second row) are shown in the appendix (Figure B1). The net effect of all individual PV tendency terms on the amplitude evolution for different phases is illustrated in Figure 11.

Overall, the quantitative agreement between the amplitude evolution of $PVA_{qL}^-$ evaluated on the pressure levels between 500 and 150 hPa and the isentropic levels between 315 and 325 K is very good (~~Fig.~~Figure 10a). The amplitude increases from March 4–16 with a peak in the amplitude in the last third of the EuBL regime life cycle. Subsequently, the $PVA_{qL}^-$ amplitude weakens until the end of its life cycle on March 25. Abrupt changes in the amplitude are due to splitting and merging events (marked at the bottom of ~~Fig.~~Figure 10a). Small qualitative differences in the evolution occur around March 7–12 when the $PVA_{qL}^-$ is located far north of higher latitudes. These differences occur because the data set used for isentropic $PVA_{qL}^-$
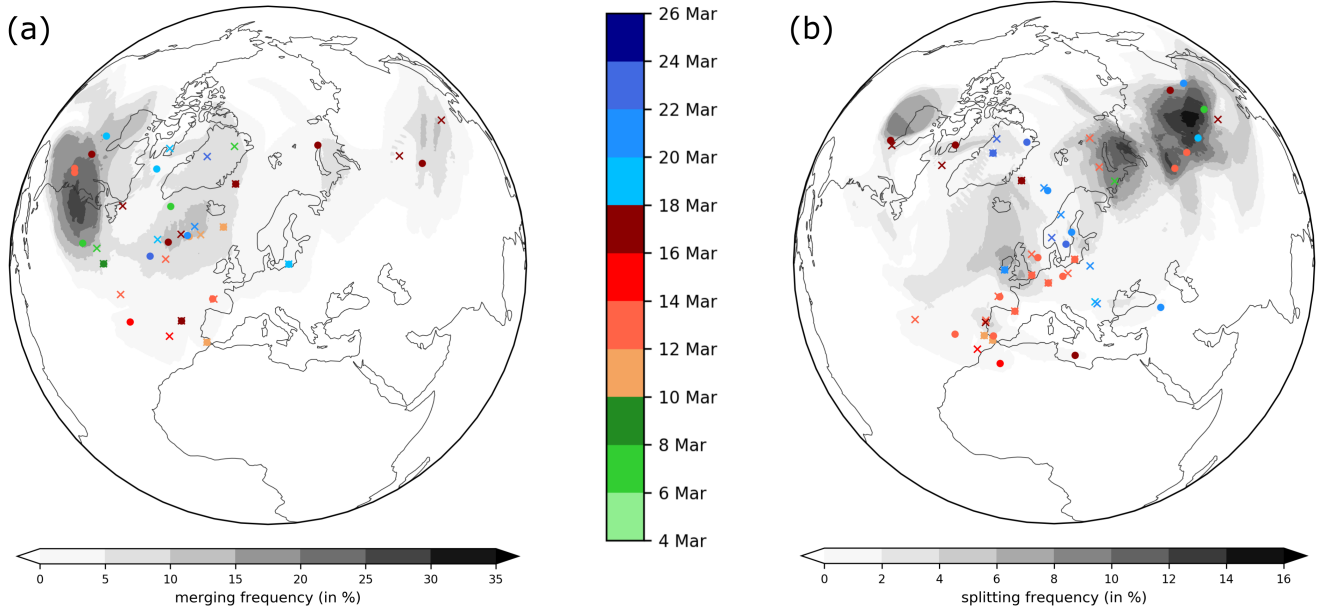
**Figure 9.** ~~Occurrence frequency (in %) of (a) PVAs$_{qL}^-$ that merge into the main contributing PVA$_{qL}^-$ and (b) PVAs$_{qL}^-$ that separate from the main contributing PVA$_{qL}^-$.~~ Occurrence frequency (in %) of (a) PVAs$_{qL}^-$ that merge into the main contributing PVA$_{qL}^-$ and (b) PVAs$_{qL}^-$ that separate from the main contributing PVA$_{qL}^-$. We consider all splitting and merging events that take place along the life cycle of the main PVA$_{qL}^-$. For the calculation per event, the PVA$_{qL}^-$ is traced back three days in case of merging or from the splitting event to three days later if possible. Crosses show the position (based on the center of mass) of the PVA$_{qL}^-$ before they merge into the main PVA$_{qL}^-$ (panel a) or at the time of splitting from the main PVA$_{qL}^-$ (panel b). Points mark the position of the PVAs$_{qL}^-$ at most three days before the merging event or at most three days after the splitting event. In case of a shorter lifetime of the PVA$_{qL}^-$ the last possible (splitting) or first possible (merging) position is shown. The color indicates the time in the life cycle at which the respective event occurs.

520   amplitude evolution is limited to 80 °N (see ~~Sect.~~Section 2.2) whereas the data set used for the pressure level based PVA$_{qL}^-$ amplitude evolution does not face these ~~limitation~~limitations. Around peak amplitude and early during the decay (March 14–20), the isentropic-based PVA$_{qL}^-$ amplitude is more pronounced than the pressure-based PVA$_{qL}^-$ which suggests that the chosen isentropic layer encloses (in particular) the strong core of the PVA$_{qL}^-$ more accurately than the layer based on pressure levels.

525     We define the first phase of the PVA$_{qL}^-$'s life cycle as the ~~period before the onset~~ **period before the onset** of the blocked regime, i.e., from March 4–9. A net amplification is evident during this phase (~~Fig.~~Figure 10b), which is by large dominated by divergent PV tendencies (~~Figs~~Figures. 10b and 11a). Two distinct episodes of intensification due to the divergent tendency occur on March 4–6 and March 7–9 (see WCB intersection points in ~~Fig.~~Figure 5a,b), both associated additionally with local maxima in the baroclinic tendencies. This signature indicates moist-baroclinic coupling (Teubler and Riemer, 2021). As further 530   discussed in ~~Sect.~~Section 4.3, both episodes are associated with prominent WCB activity of an extratropical cyclone upstream,
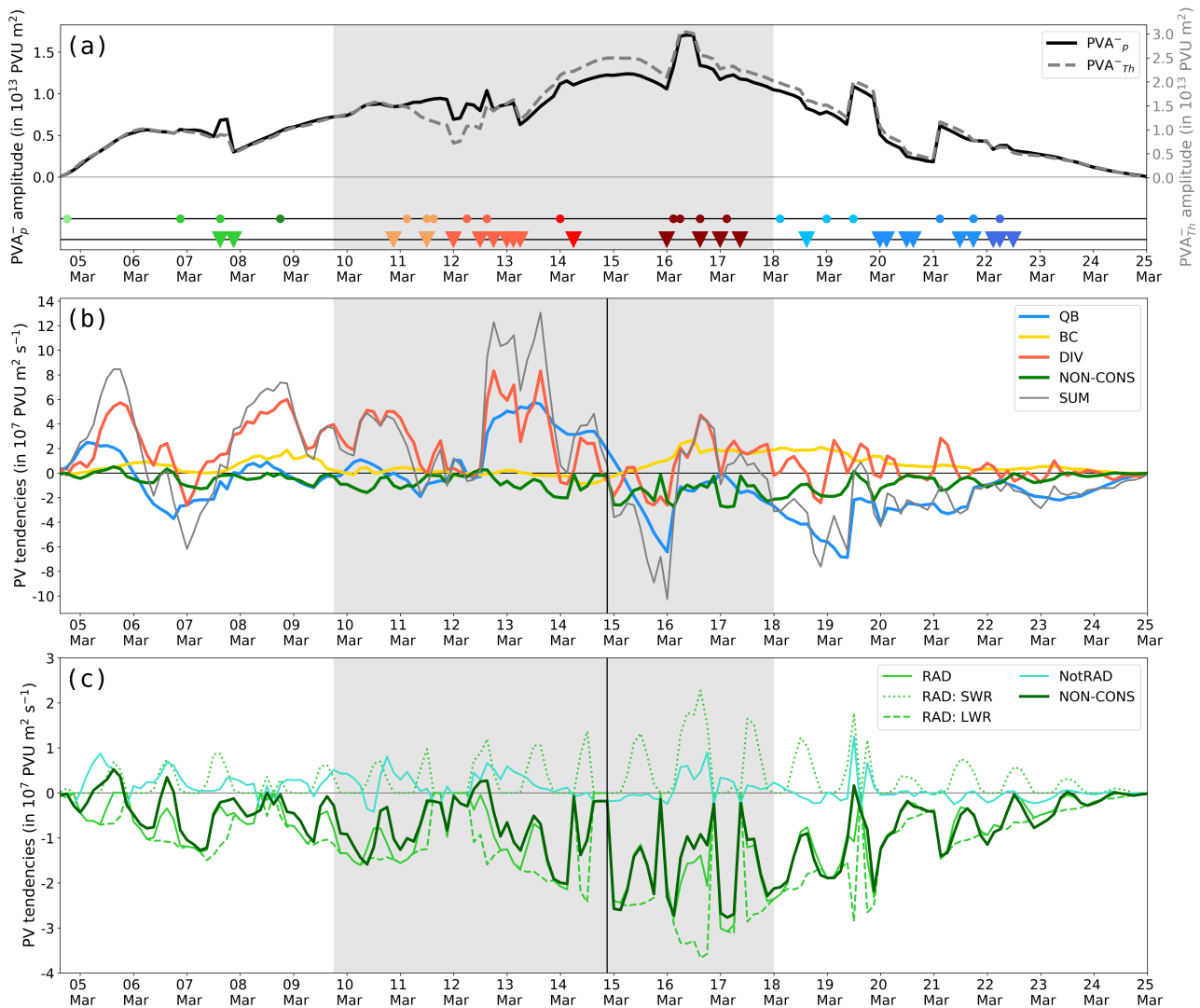
**Figure 10.** ~~Process contributions to the amplitude evolution of the main PVA$_{qL}^-$ associated with the EuBL episode in March 2016.~~ Process contributions to the amplitude evolution of the main PVA$_{qL}^-$ associated with the EuBL episode in March 2016. (a) Integrated PVA$_{qL}^-$ amplitude in terms of isentropic layer average (315–325 K, gray dashed) and pressure layer average (500–150 hPa, black solid) for the ~~life time~~ lifetime of the PVA$_{qL}^-$. Colored symbols along the two horizontal lines in the lower half of the panel mark the occurrence of splitting (triangles) and merging (dots) events. The color of the markers points to the timing of these events (see colorbar in ~~Figs.~~ Figures 8 or 9). (b) Integrated PV tendency terms for PVA$_{qL}^-$ that contribute to the PVA$_{qL}^-$ amplitude evolution: Quasi-barotropic term (QB, blue), baroclinic term (BC, yellow), divergent term (DIV, red), non-conservative term (NON-CONS, green), and the sum of all ~~four~~ terms mentioned before (SUM = QB + BC + DIV + NON-CONS, gray). (c) Division of the non-conservative PV tendency term (NON-CONS, solid dark green) into its various components: non-radiative part (NotRAD, solid turquoise) and radiative part (RAD, solid light green). The radiative term is further partitioned into the non-conservative PV tendency by shortwave radiation (RAD: SWR, dotted light green) and by longwave radiation (RAD: LWR, dashed light green). Note the sign convention here is that positive tendencies signify a strengthening of PVA$_{qL}^-$ amplitude. The period of the active EuBL life cycle is shown in all panels in gray shading and the vertical black line in (b) and (c) marks the date used to split up the EuBL life cycle in two episodes for the analysis presented in Figure 11. Note the different y-axis ranges between (b) and (c).
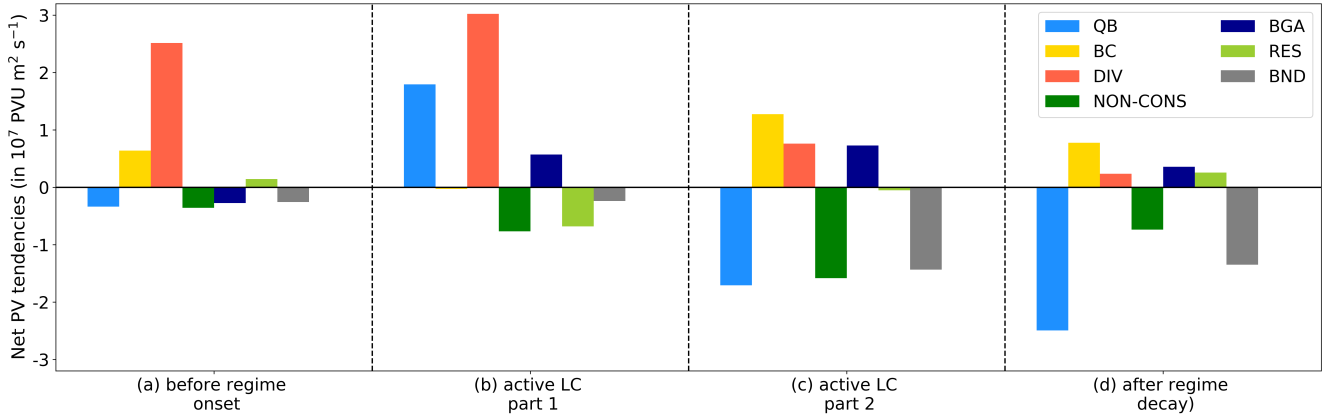
**Figure 11.** ~~Net effect of PV tendencies and splitting/merging events on the amplitude evolution of the PVA$_{qL}^-$ for different time periods within the PVA$_{qL}^-$ life time.~~ ~~Different~~ Net effect of PV ~~tendency terms~~ tendencies on the amplitude evolution of ~~Fig~~the PVA$_{qL}^-$ for different periods within the PVA$_{qL}^-$ lifetime. All contributing PV tendency terms from Equation ~~10~~ 9 (except $\partial q_0/\partial t$) are summed up over 4 different ~~time~~ periods (from left to right): (a) ~~prior to~~ before EuBL onset (March 4, 15 UTC – March 9, 15 UTC), (b) active EuBL life cycle part I (March 9, 18 UTC – March 14, 21 UTC), (c) active EuBL life cycle part II (March 15, 00 UTC – March 18, 00 UTC), and (d) after EuBL decay (March 18, 03 UCT – March 25, 00 UTC). ~~Isentropic PVA amplitudes of the splitting and merging PVAs are summed up separately for the quantification of the net effect of splitting and merging events.~~ To account for different lengths of the ~~time~~ periods, we divide the sums by the number of time steps in the period. Note that the PV tendency term $\partial q_0/\partial t$ of Equation 9 is not shown here because it is so small that it does not affect the amplitude change.

providing some evidence that the pronounced amplification due to the divergent tendency is in this case indeed coupled to latent heat release and can thus be considered as an indirect diabatic impact. Quasi-barotropic PV tendencies govern the very early amplification of the PVA$_{qL}^-$ (~~Fig.~~Figure 10b), suggesting that ~~downstream development~~ the trough sitting over the eastern part of the U.S. makes an important contribution to the formation of the incipient ~~anomaly~~PVA$_{qL}^-$ through northward advection of low PV air into the downstream region. The net impact of the quasi-barotropic tendencies during the first phase, however, is small and negative (~~Fig.~~Figure 11a), which is due to the period of negative tendencies around March 7 (~~Fig.~~Figure 10b). The net impact of ~~splitting and merging~~ the boundary term $BND$ during the first phase is ~~relatively small and negative (Fig.~~slightly negative (Figure 11a)~~, which can mostly be attributed to~~. Although the PVA$_{qL}^-$ area is growing and experiences various merging events from its first detection until the EuBL onset, the aforementioned splitting event on March ~~7.~~7 (Fi. 8b, green triangle with label 'A') seems to dominate the net effect (Figure 11a).

We define the second phase of the PVA$_{qL}^-$ life cycle as the ~~first part of the active EuBL life cycle, from March 9–15, where~~ **first part of the active EuBL life cycle** from March 9 18 UTC – March 14 21 UTC. Our motivation to define March 14 21 UTC as the end of this period is that (i) there is still an amplification of the PVA$_{qL}^-$ amplitude~~takes place. This phase ends when~~, (ii) the sum of ~~the~~ diagnosed processes in ~~Fig.~~Figure 10b turn generally negative ~~. Our second motivation to define March 15 as the~~

~~end of this period is that this date~~ after that time, and (iii) this choice delineates two periods with several splitting and merging events ~~. This~~ within the active regime life cycle. In general, this first part of the active regime life cycle is associated with a further general amplification of the PVA$_{qL}^-$ (~~Fig.~~Figure 10b and ~~Fig.~~Figure 11b). Same as before the onset, two major episodes occur during which the sum of the diagnosed processes indicate prominent amplification. The first episode occurs just after the onset of the regime life cycle (March 10–11) and the other from March 13–15 (~~Fig.~~Figure 10b). ~~The~~ Again, the divergent PV tendency ~~dominates the first episode and makes a prominent~~ term highly dominates both amplification episodes. However, the quasi-barotropic PV tendency makes an important additional contribution to the ~~second episode, which is dominated by the quasi-barotropic PV tendency~~ already strongly pronounced divergent PV tendencies in the second episode (March 13–15). Throughout the entire PVA$_{qL}^-$ life cycle, both tendency terms show a clear maximum contribution from March 13–15. The net effect of both~~tendencies are of equal importance for amplification during the second phase (Fig.~~, divergent and quasi-barotropic PV tendencies is positive with a distinct stronger net effect in the divergent PV tendencies pointing to the importance of moist processes in the first part of the active EuBL regime life cycle (Figure 11b). The baroclinic PV tendency has a negligible impact in this phase ~~, whereas the net impact of splitting and merging is large and negative . We attribute this negative impact to a strong~~ with no net effect at all. The net effect of $BND$ is again negative and rather small as for the first phase prior to onset. A variety of splitting and merging events take place (Figure 8b, Figure 10a) that lead to huge values in the second term within $BND$ that describes the PVA$_{qL}^-$ area change by the movement of the boundary. The major splitting event on March 13 (~~Fig.~~Figure 8b)~~.~~, the orange triangle with label 'B') is most probably responsible for the net weakening effect of $BND$. Note that the rather high signal of $RES$ might be attributed to the fact, that the PVA$_{qL}^-$ area extends north of the PV inversion region where marginal effects of the piecewise PV inversion arise (Figure 11b, Figure B1b).

The ~~remainder of the active blocked regime life cycle~~ **second part of the active blocked regime life cycle** (March 15–18) ~~,~~ is characterized by a negative net impact of the diagnosed tendencies (~~Fig.~~Figure 10b, Figure 11c). This net impact heralds the eventual decay of the PVA$_{qL}^-$. In contrast to the first part of the active life cycle, the quasi-barotropic tendency now makes a major contribution to the weakening of the PVA$_{qL}^-$. The baroclinic tendency, negligible during the first part of the active life cycle, turns persistently positive after the quasi-barotropic tendency turns negative on March 15, and thus constitutes the main contribution to counteracting the weakening of the PVA$_{qL}^-$ (~~Fig.~~Figure 10b) in ~~this second part .~~ the second part of the regime life cycle. This positive contribution of baroclinic PV tendencies leading to the amplification of PVA$_{qL}^-$ indicates incipient downstream moist-baroclinic development (more on this in Sections 5.1 and 5.2 in Teubler and Riemer (2021)). The divergent PV tendency is of less importance than before ~~, with only~~ but still shows a small positive net impact (~~Fig.~~Figure 11c). The ~~net effect~~ $BGA$ term that describes the advection of background PV with the background wind has a negligible but consistently positive effect on the PVA$_{qL}^-$ amplitude (Figure B1b) resulting in an overall positive net effect to the strengthening of the PVA$_{qL}^-$ amplitude. In contrast to the two phases before, $BND$ has a strong negative net effect in the second part of the active regime life cycle (Figure 11c). Generally, strong deformation of the PVA$_{qL}^-$ occurs during this phase (not shown) that is accompanied by several splitting and merging events, which contribute to sudden noticeable changes in amplitude but also to substantial relative changes in the area ~~of splitting and merging is again negative and dominates the weakening, mainly attributable to two~~

~~splitting events during which large parts of~~ the PVA$_{qL}^-$ ~~cut off (Fig.~~ between 30 and 50 % (in particular the two splitting events C1 and C2 and the merging event D in Figure 8b).

In the ~~final decay phase~~ **final decay phase** of the PVA$_{qL}^-$ (March 18–25), most of the tendencies exhibit similar characteristics as during the second part of the active life cycle. The quasi-barotropic tendency contributes strongly to the weakening ~~, whereas the baroclinic and divergent tendencies make small positive contributions (Figs.~~ most probably because of the beginning deformation of the PVA$_{qL}^-$ after the regime decay. The divergent and in particular the baroclinic tendencies make positive contributions which decay strongly in the last days before the end of the PVA$_{qL}^-$ life cycle (Figure 10b~~and~~, Figure 11d). ~~Although the number of~~ The $BND$ term again exhibits a strong negative net effect after regime decay pointing to a degrading contribution as the PVA$_{qL}^-$ decreases in size towards the end of the PVA$_{qL}^-$ life cycle (not shown). Several splitting and merging events ~~is now the largest in all phases (Fig.~~ take place, with the number of splitting events predominating (Figure 8b)~~, these events balance each other almost completely and their net impact in the phase shortly after the regime decay is negligible~~.

**Direct diabatic impact**

The direct diabatic tendency, i.e., the direct impact of non-conservative processes, is predominately negative and the absolute value is in general smaller than that of the advective PV tendencies throughout the life cycle (~~Fig.~~Figure 10b). Longwave radiation dominates this direct diabatic weakening of the PVA$_{qL}^-$ (~~Fig.~~Figure 10c), as expected from idealized considerations (Zierl and Wirth, 1997) and consistent with the impact of longwave radiative cooling on ridges within Rossby wave packets (Teubler and Riemer, 2021). Teubler and Riemer (2021) provided a rough estimate that ~~one third~~ one-third of the longwave radiative tendencies may be associated ~~to~~ with cloud-radiative effects, whereas the majority of the signal was interpreted as a large-scale 'background' signal. In addition, these authors demonstrated that the longwave radiative tendency roughly scales with the amplitude of the PVA, which is consistent with the observed minimum of the tendencies at the peak time of PVA$_{qL}^-$ during the second part of the active EuBL regime life cycle. Shortwave radiation counteracts the weakening and, unsurprisingly, exhibits a distinct diurnal cycle.

The non-radiative diabatic tendencies are mostly positive. The dominant amplifying diabatic tendencies within ridges are due to latent heat release (e.g., Chagnon et al., 2013; Teubler and Riemer, 2021), suggesting that latent heat release has a (small) positive *direct* impact on the onset of the EuBL regime life cycle in March 2016 also. The overall net impact of all direct diabatic tendencies on the amplitude evolution is, however, negative and ~~non-negligible compared to~~ smaller than the net impact of the advective tendencies (~~Fig.~~Figure 11).

**Synopsis of the quasi-Lagrangian perspective**

The main PVA$_{qL}^-$ associated with the EuBL regime life cycle in March 2016 was first identified by our tracking algorithm off the U.S. East Coast five days ~~prior to~~ before regime onset. Moving towards northern Europe, the PVA$_{qL}^-$ underwent several splitting and merging events. The net impact of these events was to weaken the amplitude of the PVA$_{qL}^-$. The divergent PV ten-

dency term dominated all amplification episodes of the $\text{PVA}_{qL}^-$ with a further substantial contribution by the quasi-barotropic tendency within the active regime life cycle. The quasi-barotropic tendency later dominates the weakening of the $\text{PVA}_{qL}^-$, counteracted by the baroclinic tendency, which becomes most relevant during the second half of the life cycle.

The by far dominant role of the divergent PV tendency in the amplification of the $\text{PVA}_{qL}^-$ before the EuBL onset quantitatively supports the findings by Magnusson (2017) and Grams et al. (2018), who argued more qualitatively that divergent WCB outflow was crucial for the onset of the block. The next section will focus in more detail on the link between the divergent PV tendency and latent heat release in WCBs from the Lagrangian perspective.

### 4.3 Lagrangian perspective

Here we investigate (i) the importance of WCB outflow and, more generally, (ii) the importance of latent heat release by backward trajectories starting in the $\text{PVA}_{qL}^-$ from the quasi-Lagrangian perspective, following Pfahl et al. (2015) and Steinfeld and Pfahl (2019). Importance is assessed by the fraction of backward trajectories that fulfill specified criteria. The criteria that define WCB outflow are given in Section 2.6. For (ii), diabatically 'heated trajectories' are defined as trajectories that experience a $\Delta\theta > 2$ K. Figure 12a compares the divergent PV tendencies from the quasi-Lagrangian perspective integrated over the $\text{PVA}_{qL}^-$ area (red) with the fraction of heated trajectories (black) and the fraction of WCB outflow (shading).

All three quantities are positively correlated over the lifetime of the $\text{PVA}_{qL}^-$ with a correlation factor between divergent PV tendencies and the fraction of heated trajectories of 0.44, between divergent tendencies and the fraction of WCB outflow of 0.57, and between the fraction of heated trajectories and the fraction of WCB outflow of 0.73. These positive correlations support the common expectation that the modification of the tropopause by upper-tropospheric divergent flow is enhanced by latent heat release in WCBs and represent a direct quantitative link between WCBs and reinforcing divergent PV tendencies within the $\text{PVA}_{qL}^-$. Most importantly, all prominent peaks of the divergent PV tendency ($> 3 \cdot 10^7$ PVU m$^2$ s$^{-1}$, grey horizontal line in Figure 12a) are associated with a WCB outflow fraction of at least 20 %, and vice versa. For the presented case, we can thus demonstrate with a high degree of certainty that the divergent PV tendencies are indeed an indirect moist impact and that the WCB outflow dynamically modifies the tropopause. In some periods within the $\text{PVA}_{qL}^-$ life cycle (e.g., March 21–23), we find a high fraction of heated trajectories, but the divergent PV tendency is relatively low or even contributes to amplitude weakening (Figure 12a). One explanation is that the timing and in particular the exact location where diabatic heating occurs along the three-day trajectory is essential, as this ultimately shapes the effect on the PV distribution within the $\text{PVA}_{qL}^-$. Thus, if the trajectory experiences the ascent and thus the period of maximum heating so early that it reaches the upper troposphere outside of the $\text{PVA}_{qL}^-$ and migrates nearly horizontally into the PV anomaly, the effect on the amplitude amplification is much smaller than if the trajectory experiences its ascent directly in the immediate vicinity of the $\text{PVA}_{qL}^-$.
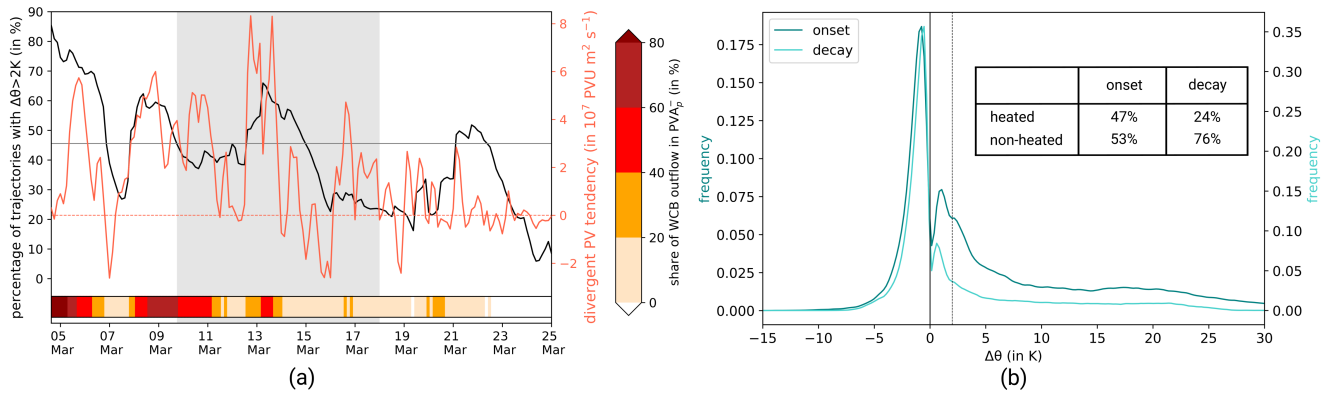
**Figure 12.** ~~Results of the Lagrangian perspective on the PV dynamics of the EuBL regime life cycle in March 2016.~~ Results of the Lagrangian perspective on the PV dynamics of the EuBL regime life cycle in March 2016. (a) Evolution of divergent PV tendencies from ~~Fig.~~ Figure 10b (red line), the fraction of heated ($\Delta\theta > 2$ K) three-day backward trajectories starting in $\mathrm{PVA}_{qL}^-$ (black), and the fraction of WCB outflow within the in $\mathrm{PVA}_{qL}^-$ area (red shading, horizontal bar). Note that the divergent PV tendencies are integrated within the $\mathrm{PVA}_{qL}^-$ area for grid points with PVA<0 PVU on the respective isentropic surfaces while WCB outflow and the backward trajectories are included for all grid points within the $\mathrm{PVA}_{qL}^-$ area and ~~for~~ latitudes < 80 °N and > 25 °N. The gray shaded area denotes the time of the active EuBL regime life cycle. See the text for the explanation of the thin grey horizontal line. (b) Frequency distribution of maximum heating and cooling rates along three-day backward trajectories starting in $\mathrm{PVA}_{qL}^- \pm$ one day around the onset (dark turquoise) and decay (light turquoise) of the EuBL. The vertical line (black, dashed) corresponds to the 2 K value. The table provides information on the proportion of heated ($\Delta\theta > 2$ K) and non-heated ($\Delta\theta < 2$ K) trajectories.

We further follow Steinfeld and Pfahl (2019) and investigate the distribution of the maximum heating and cooling rates along the ~~trajectories~~ three-day backward trajectories that are started from the $\mathrm{PVA}_{qL}^- \pm$ one day around the onset and decay of the EuBL (~~ Fig~~ Fig 12b). ~~We additionally~~ Additionally, we analyze the spatial origin of the diabatically heated and non-heated

650 ~~three-day backward trajectories ending in the $\mathrm{PVA}_{qL}^-$ (Fig.~~ backward trajectories separately (Figure 13). As in Steinfeld and Pfahl (2019), we see a broad heating regime with values as high as $\Delta\theta > 20$ K within 3 days and a narrow non-heated regime with values as low as $\Delta\theta < $ -5 K. Most three-day backward trajectories (53 % around the onset and 76 % around the decay) experience diabatic cooling ~~prior to their arrival~~ before they arrive in the $\mathrm{PVA}_{qL}^-$, most probably due to longwave radiative cooling. Around the EuBL onset, a high fraction of these air parcels ~~are~~ is located upstream of the $\mathrm{PVA}_{qL}^-$ in the mid or upper

655 troposphere and probably reach the $\mathrm{PVA}_{qL}^-$ by adiabatic advection (~~Fig.~~ Figure 13b). In comparison, we see in ~~Fig.~~ Figure 13d in addition to the adiabatic advection of air parcels from upstream some recirculating air parcels in the upper troposphere that are already located within or near the ~~the~~ $\mathrm{PVA}_{qL}^-$.

The substantially increased fraction of heated trajectories around onset (47 %) as compared to around decay (24 %) in ~~Fig.~~ Figure 12b demonstrates the importance of diabatic heating for the development and strengthening of the $\mathrm{PVA}_{qL}^-$ in an

660 earlier stage of the life cycle from the Lagrangian perspective. ~~With respect to~~ Concerning the spatial origin of the heated trajectories, we identify the southern North Atlantic as a key source region around the EuBL onset and decay (~~Fig.~~ Figure 13a,c).
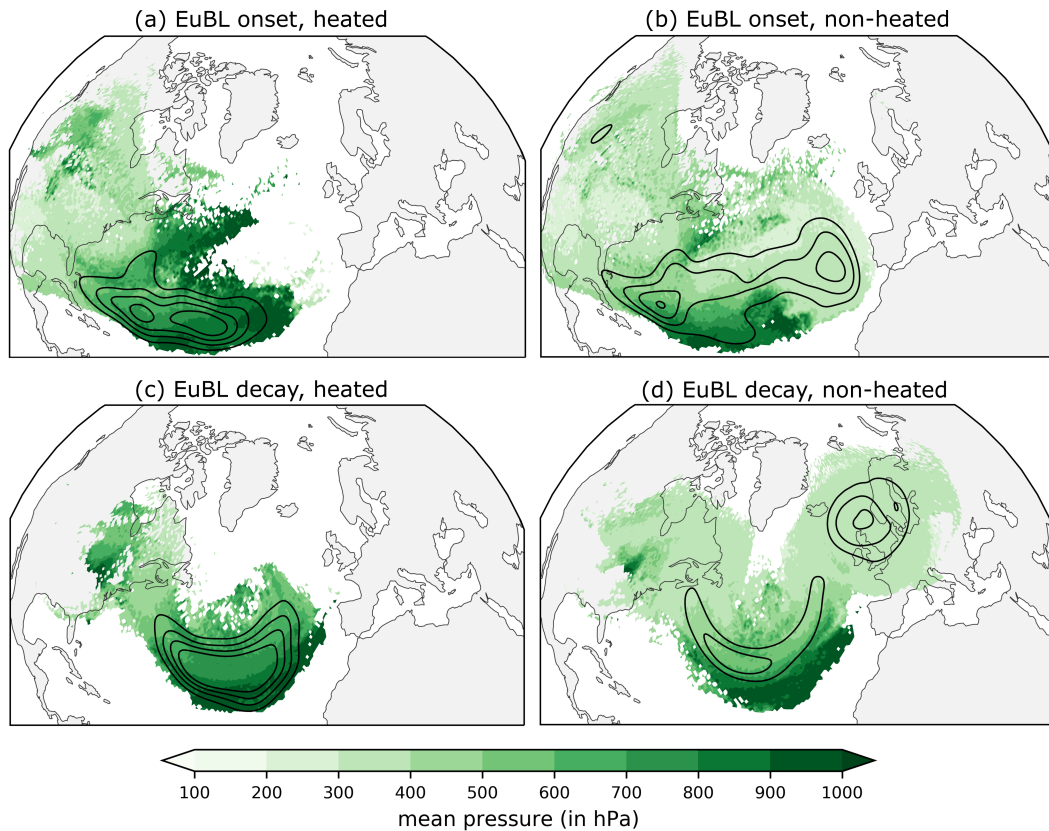
**Figure 13.** ~~Origin of air parcels that end up in the PVA$_{qL}^{-}$ around the EuBL onset (upper row) and the decay (lower row).~~ Origin of air parcels that end up in the PVA$_{qL}^{-}$ around the EuBL onset (upper row) and the decay (lower row). The origin of air masses is shown separately for diabatically heated trajectories ($\Delta\theta > 2$ K) and non-heated trajectories. We take into account all three-day backward trajectories out of the PVA$_{qL}^{-}$ in the time window $\pm$ one day ($\Delta t = 3$h) around the EuBL onset and decay. ~~Pressure~~ The pressure of the air parcels associated with the trajectory (in hPa) is shown at time t = -3 days in green shading. If there are several air parcels at the same grid point (by considering several times), we display the mean pressure. The occurrence frequency is shown in black contours for the heated trajectories in steps of 1.5, 2.5, 3.5 and 4.5 $10^{-2}$ and for the non-heated trajectories in steps of 1.0, 1.5, 2.0, 2.5 $10^{-2}$. For a clearer visualization ,the field has been Gaussian filtered with $\sigma = 4$. See ~~Sect.~~Section 2.6 for more information on the backward trajectory calculations.

The position of air parcels upstream of the PVA$_{qL}^{-}$ in the lower troposphere suggests that air parcels will most probably experience latent heat release on their ascent to the upper-tropospheric PVA$_{qL}^{-}$ in the following three days.

The Lagrangian perspective thus complements what was learned from the quasi-Lagrangian perspective and links the amplitude-enhancing divergent PV tendency contribution from the quasi-Lagrangian perspective to the occurrence of latent heating (mostly) associated with the occurrence of WCBs, which represents an important contribution, especially around the EuBL onset.

665

## 5 Synopsis and discussion

Here we discuss the three perspectives' different insights into the dynamics of the EuBL regime life cycle in March 2016 and compare our findings to previous studies. In this context, we will bring together the perspectives combined as a novel diagnostic framework for selected regime life cycle stages.

The PVAs that compose the EuBL regime pattern are advected into the region and do not build up locally over Europe. From the Eulerian perspective, the quasi-barotropic PV tendency term is the dominant contributor in the regime onset phase. The term contains two distinct processes that describe (i) the downstream PV advection by the background flow and (ii) the propagation and advection into the region by intrinsic phase velocity. In this case, the downstream PV advection by the background flow is of greater importance. This result is in line with Michel and Rivière (2011), who investigate the processes associated with transitions between different weather regimes using a ~~streamfunction~~ stream function tendency equation. Similarly to our case, they highlight the importance of the propagation of low-frequency anomalies for the transition from a zonal to a blocked regime. In the quasi-Lagrangian perspective, the term describing the advection of anomalies is eliminated as we follow the main $\mathrm{PVA}_{qL}^-$ associated with the regime life cycle. However, the track of the $\mathrm{PVA}_{qL}^-$ indirectly informs about advection and provides important complementary spatial information which reveals that the $\mathrm{PVA}_{qL}^-$ migrates from the U.S. East Coast into the European region from upstream.

All three perspectives identify an ~~important~~ amplifying role of moist dynamics in the **onset** of the EuBL regime life cycle. From the quasi-Lagrangian perspective, pulse-like amplification phases are associated with the divergent PV tendency term in the period from the onset of the $\mathrm{PVA}_{qL}^-$ to the regime onset representing a strong indirect moist contribution. This is confirmed by the results of the Lagrangian perspective, which show that a high fraction of the backward trajectories has a diabatic history in which air parcels ending in the $\mathrm{PVA}_{qL}^-$ were heated in the days before. Our insights into the processes at the regime onset fit well with the results of Pfahl et al. (2015) and Steinfeld and Pfahl (2019), who investigate the role of latent heat release in atmospheric blocking. They find that moist-diabatic processes play an important role during the onset of blocking, which we can confirm for our case study. In contrast, the divergent indirect moist processes do not emerge quite as prominently in the Eulerian low-frequency perspective. Even when the regime pattern is split into negative and positive PVAs, the divergent term indicates a reinforcing contribution but does not stand out as a major contributing process. ~~One reason for this is the filtering out of sporadic synoptic activity associated with moist processes~~ While the low-pass filtering in the Eulerian ~~low-frequency perspective. The~~ framework may contribute to these differences, the main reason, however, is that the Eulerian perspective quantifies the in-situ evolution of the regime pattern over Europe such that moist dynamics occurring upstream are missing and only indirectly captured by the quasi-barotropic PV tendency term. Overall, the importance of processes on different scales fits well ~~to~~ with the findings of Woollings et al. (2018), who point to the interplay of processes on planetary and synoptic scales in blocking onset.

The **maintenance** of the regime, ~~with respect to~~ concerning the anticyclonic anomaly, is caused, among other things, by moist synoptic activity upstream that contributes to the maintenance or even further amplification of the $PVA_{qL}^-$. A high fraction of the backward trajectories from the $PVA_{qL}^-$ has a diabatic history from a Lagrangian perspective and divergent PV tendencies contribute to an amplification of the $PVA_{qL}^-$ from a quasi-Lagrangian perspective. Heating appears as an indirect effect that leads to an increase in transport of ~~low-level~~low-tropospheric, low-PV air up the WCB into the $PVA_{qL}^-$, consistent with Methven (2015). The moist processes that now occur locally near the regime mask compared to the onset (where they occur further upstream outside of the regime mask) are reflected in peaks of the divergent PV tendencies in the Eulerian perspective. These results are in good agreement with the climatological study of Steinfeld and Pfahl (2019) who point to multiple episodes of latent heating 'bursts' that lead to the re-intensification and growth of an existing block during the maintenance stage of its life cycle. Baroclinic PV tendencies play a positive, but subordinate role during regime onset but become more important for the maintenance. In an energy framework, and on average over many winter cases, Martineau et al. (2022) found that baroclinic energy conversion makes a leading-order contribution to the energetics of Greenland blocks. Individual tendency terms in an energy framework and a PV framework are not directly comparable (e.g., see discussion in Section 3f of Wirth et al., 2018b) and a single case study cannot be compared to the mean results of many cases. It is worth pointing out, however, that our analysis focuses on the upper troposphere, whereas Martineau et al. (2022) find the strongest signal in the low to middle troposphere. In addition, we stress that our analysis demonstrates the importance of moist-baroclinic growth for the amplification of the $PVA_{qL}^-$ before and during onset. It is the divergent outflow associated with moist processes below, however, that is most effective in amplifying the upper-level anomaly in our case study. We thus consider our results to be consistent with those of Martineau et al. (2022). The attraction and absorption of a synoptic-scale anticyclonic eddy by the block as a maintenance mechanism is a well-known concept (Yamazaki and Itoh, 2009) and is here investigated in the quasi-Lagrangian perspective. The tracking algorithm that considers splitting and merging events detects several merging $PVAs_{qL}^-$ from the southwest that amplify the existent main $PVA_{qL}^-$ over Europe. More than 50 % of the merging events identified around the EuBL occur within the regime life cycle and provide evidence that these merging events are important for maintaining or re-intensifying the $PVA_{qL}^-$ strength. However, a few splitting events in the maintenance stage are associated with noteworthy effects on the amplitude and area of the $PVA_{qL}^-$ and dominate the net effect on the $PVA_{qL}^-$ amplitude for the active life cycle stage. Nevertheless, with the novel tracking algorithm, it is for the first time possible to quantify the well-known concept of Yamazaki and Itoh (2009).

The **decay** of the EuBL regime pattern is associated with the advection of the $PVA_{qL}^-$ out of the region and the absence of moist processes that could maintain the anticyclonic part of the regime. Slow amplitude reduction of the traced $PVA_{qL}^-$ in the quasi-Lagrangian perspective starts in the second half of the regime life cycle. Here, the quasi-barotropic tendency term has the key role and leads the decay. We further assume that nonlinear processes (which are included in the eddy term in the Eulerian perspective) make a non-negligible contribution ~~in~~ to the decay of the regime. This is in high agreement with the results of Michel and Rivière (2011), which pointed to the importance of nonlinear processes in the transition stage from blocking over the eastern North Atlantic to a blocked regime more towards the west, as we see it in the case here that transitions towards an Atlantic Ridge regime. ~~In addition, both perspectives~~Large deformations, which can occur in the context of nonlinear

processes, are often associated with splitting events. And indeed, the impacts of splitting events dominate over the merging events around the decay stage and provide an important contribution to the degradation of the $PVA_{qL}^-$. Both, the Eulerian and quasi-Lagrangian perspectives, show that the divergent PV tendency term plays a ~~very~~ more minor role in the decay phase~~and even contributes to the decay of the regime pattern~~. The absence of moist processes is visible in the Lagrangian perspective by the low fraction of heated backward trajectories and matches very well with Steinfeld and Pfahl (2019), who point to reduced moist processes during the decay phase of a block. Overall, both fit the hypothesis of Hoskins (1997) that the disruption by the advection of other systems and the lack of a maintenance process can be associated with the decay of a block.

## 6    Concluding remarks

The present study introduces three different perspectives on how to quantify the PV dynamics of blocked weather regime life cycles in the North Atlantic-European region based on ERA5 reanalysis data. The Eulerian, quasi-Lagrangian and Lagrangian perspectives on regime dynamics are applied to a EuBL regime life cycle that occurred from March 9–18 2016. This case is motivated ~~from~~ by the fact, that its onset was associated with a forecast bust at ECMWF. We show that each of the perspectives can stand alone but that a combined usage ~~is able to~~ can provide a much more complete picture of the dynamics. A ~~particular~~ particularly novel aspect is the quasi-Lagrangian perspective, which helps to bridge the gap between the Lagrangian and Eulerian perspectives through the tracking of negative, upper-tropospheric PVAs ($PVAs_{qL}^-$) and the use of the Eulerian PV tendencies to investigate the amplitude evolution of $PVAs_{qL}^-$. These PV tendencies enable us to distinguish the importance of dry and moist processes in the different life cycle stages and thus a deeper insight into the dynamics.

The Eulerian perspective shows that the onset and maintenance of the EuBL pattern in March 2016 can be described predominantly by barotropic wave propagation namely, the advection of PVAs by the upper-tropospheric flow into the region where the block establishes. A split-up into anticyclonic and cyclonic PVAs of the full patterns demonstrates the importance of the divergent PV tendency as the second largest contribution in the establishment of anticyclonic PVAs indicating the potential relevance of moist processes. Since the Eulerian perspective only considers the processes that occur within a specified region, it misses the processes that cause the formation of the PVAs upstream. This information is obtained from the quasi-Lagrangian perspective that identifies and follows $PVAs_{qL}^-$. The traced $PVA_{qL}^-$ that occupies the anticyclonic part of the regime pattern originates near the U.S. East Coast five days prior to the regime onset and migrates northeastward. An analysis of the $PVA_{qL}^-$ amplitude evolution shows the pulse-like amplification before and during the EuBL life cycle, which results almost exclusively from divergent and quasi-barotropic PV tendencies. Using the Lagrangian perspective with backward air parcel trajectories emerging from the traced $PVA_{qL}^-$, we confirm the relationship between the divergent PV tendency and diabatic contributions to the $PVA_{qL}^-$ amplitude evolution. When pulse-like $PVAs_{qL}^-$ amplitude amplification occurs mainly due to the divergent PV tendency, we find a high fraction of heated trajectories ending in the $PVA_{qL}^-$ at the same time. In addition, it is shown that the pulse-like amplifications of the $PVA_{qL}^-$ are related to WCBs, which can lead to a strong divergent outflow and the modification of the upper-tropospheric PV distribution. Hence, our results ~~here~~ provide evidence that the divergent PV tendency term in the PV framework of Teubler and Riemer (2016) can indeed be interpreted as an indirect diabatic effect.

The Eulerian perspective has the advantage that it directly quantifies the processes leading to the weather regime index. Although it misses the synoptic activity upstream of the regime pattern, it takes into account the evolution of the full pattern which is in contrast to the quasi-Lagrangian and Lagrangian perspectives that focus exclusively on the dominant anticyclonic regime anomaly. Hence, the multi-perspective analysis is important to understand the full regime evolution. If not considered together, some kind of consideration of the cyclonic part of the regime pattern should be included from a pure quasi-Lagrangian perspective as it helps to obstruct the westerly flow and is therefore related to the impact of blocked regimes.

However, by unifying the three perspectives on blocked regime dynamics within the theoretical concept of PV thinking, our novel framework enables - for the first time - a holistic view ~~on~~ of the dynamics of blocked weather regimes in particular including a quantification of the contribution of moist processes in different life cycle stages. The perspectives introduced here form a foundation for a systematic analysis of blocked regime dynamics. ~~A~~ The next step will be a climatological investigation of blocked regime life cycles in ERA5 which addresses the dynamics of the three different life cycle stages (onset, maximum stage, decay) from the quasi-Lagrangian perspective. Once a few adjustments have been made to the framework (such as developing a year-round threshold and sensitivity tests of the chosen parameters), it can be systematically applied to all blocked regime life cycles in ERA5. It is of interest to study which processes are important in the buildup of the negative PVA of the blocked regime and by which processes the block is maintained and kept stationary. Furthermore, we plan to address the dynamics of the decay process of blocked regime life cycle patterns. The quasi-Lagrangian perspective developed here could be the key tool to test and verify many theories of blocking dynamics (e.g. ~~also the eddy-training~~ the eddy-straining idea of Shutts (1983)) for a variety of blocked regime life cycles.

*Code availability.* The used codes from this study can be provided by the authors upon request.

*Data availability.* ERA5 reanalysis data can be downloaded from the ECMWF webpage (https://www.ecmwf.int/en/forecasts/datasets/reanalysis-datasets/era5, European Centre for Medium-Range Weather Forecasts, 2022).
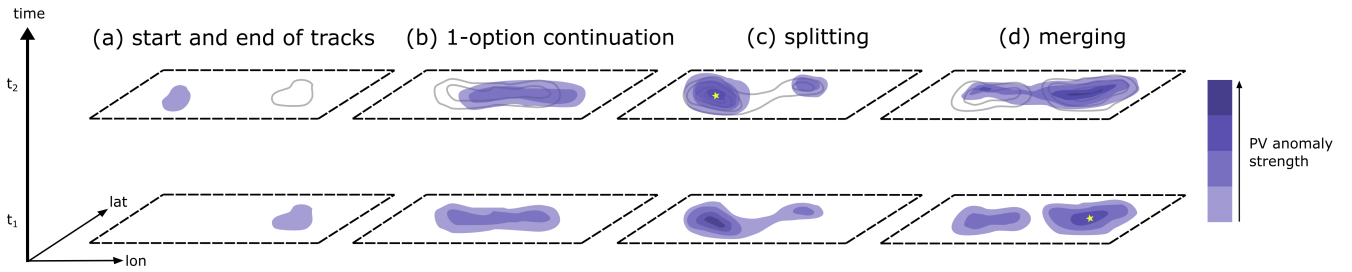
**Figure A1.** ~~Schematic of the 2D tracking algorithm applied to PVAs$_{qL}^-$ in the quasi-Lagrangian perspective.~~ Schematic of the 2D tracking algorithm applied to PVAs$_{qL}^-$ in the quasi-Lagrangian perspective. The sketch demonstrates the development of a PVA$_{qL}^-$ object (blue shading) from one time step ($t_1$) to the next ($t_2$) upwards for different situations: (a) start and end of a track, (b) 1-option continuation, (c) splitting, and (d) merging. The gray thin lines in the upper row at $t_2$ indicate the position and amplitude of the PVA$_p^-$ object at $t_1$ to show the overlap more visually. Yellow dots in panels (c) and (d) indicate which tracking ID is continued between the time steps, which means that one PVA$_{qL}^-$ object gets a new tracking ID (in case of splitting) or a tracking ID ends (in case of merging).

## Appendix A: Details on the tracking algorithm in the quasi-Lagrangian perspective

This novel contour overlap tracking algorithm traces 2D structures and captures the full life cycle of the identified PVAs$_{qL}^-$ (in the quasi-Lagrangian perspective), considering splitting and merging that occur during the life cycle. Here the algorithm determines the number of PVAs$_{qL}^-$ that spatially overlap the PVA$_{qL}^-$ object identified in the time step before. A count of zero

795    indicates the end of the PVA$_{qL}^-$ life cycle (~~Fig.~~Figure A1a). A simple continuation of the track takes place if only one single PVA$_{qL}^-$ shows an overlap (~~Fig.~~Figure A1b). A splitting event is diagnosed when the count is greater than one (~~Fig.~~Figure A1c). A merging event takes place if multiple PVAs$_{qL}^-$ show a spatial overlap with the same PVA$_{qL}^-$ object one time step later (~~Fig.~~Figure A1d). Since the life cycle of a PVA$_{qL}^-$ should not end automatically due to these splitting and merging events, the integrated PVA$_{qL}^-$ amplitude of the PVAs$_{qL}^-$ decides which PVA$_{qL}^-$ object continues the tracking ID. The other involved

800    PVA$_{qL}^-$ objects get new tracking IDs (in case of splitting) or the track of a smaller, weaker PVA$_{qL}^-$ feeding into a larger, stronger PVA$_{qL}^-$ ends with the merging event. Simultaneous splitting and merging events are also detected by the algorithm and evaluated accordingly. The output of the tracking algorithm contains the PVA$_{qL}^-$ tracks and additionally saves the information on splitting and merging events occurring along the track. This also makes it possible to determine not only the beginning of the track but also the local origin of PVAs$_{qL}^-$.

805    ## Appendix B: Computation of the boundary term and comparison of the diagnosed and observed PVA$_p^-$ amplitude evolution in the quasi-Lagrangian perspective

The ~~boundary term $Bnd$ in Eq.~~second term in $BND$ in Equation ~~??~~ 9 is very difficult to evaluate accurately. ~~First of all, the~~ The movement of the boundary $\boldsymbol{v}_s$ is essentially unknown, and $|\boldsymbol{v}_s|$ becomes very large when merging or splitting occurs. ~~Second, while $\nabla \cdot (q'\boldsymbol{v})$ can easily be computed, this term tends to have large gradients near the boundary of PVAs (not shown), i.e.,~~

810 ~~the integration over the area $A$ of the PVA$_{qL}^{-}$ may depend sensitively on that exact location of the boundary. In addition, $\boldsymbol{v}_s$ and $\boldsymbol{v}$ tend to be large but partially compensate each other, making the calculation prone to numerical inaccuracy.~~

~~We consider the part of $Bnd$ that involves $\boldsymbol{v}_s$ in the form $\int_{\mathcal{A}} \boldsymbol{\nabla} \cdot (q'\boldsymbol{v}_s)dA$.~~ To estimate this term we note that $\boldsymbol{\nabla} \cdot \boldsymbol{v}_s$ signifies a change of area $\Delta\mathcal{A}$ of the PVA$_{qL}^{-}$. Assuming a constant value $\overline{q}$ of $q'$ at the boundary we can estimate $\int_{\mathcal{A}} \boldsymbol{\nabla} \cdot (q'\boldsymbol{v}_s)da \approx \overline{q}\Delta\mathcal{A}$. We choose $\overline{q}$ as the average of $q'$ along the boundary. The value for $\Delta\mathcal{A}$ is taken from the observed area change of the PVA$_{qL}^{-}$.

815 ~~Using these assumptions, we are able to~~

By taking into account the sum of all tendency terms on the RHS of Equation 9 and comparing it with the observed amplitude change, ~~we can~~ close our $q'$ budget to a very high degree (~~Fig.~~Figure B1). Note that the ~~prominent spikes indicate splitting and merging events~~missing tendency terms that are not displayed in Figure 10 are shown for the sake of completeness in

820 Figure B1b. It appears that $BND$ dominates the overall change in PVA amplitude (Figure B1a) due to the prominent spikes in $BND$ (Figure B1a). These spikes indicate abrupt changes in the PVA$_{qL}^{-}$ area, which we ~~quantify more accurately by using the information from tracking algorithm that is~~ can assign more accurately to splitting and merging events identified by the novel quasi-Lagrangian tracking algorithm discussed in detail in ~~Sects.~~Sections 4.2 and A. ~~Within three periods~~

825 Occasionally, the diagnosed PV tendencies do not reproduce the observed evolution sufficiently well ~~. The first occurs around March 7 when a substantial portion of the extensive northward~~ (Figure B1a). This can occur for example around March 7–8 and March 12–14 when the PVA$_{qL}^{-}$ ~~splits off and moves north~~ extends northwards of 80 °N ~~out of~~ and is partly located outside the domain to which we restrict our piecewise PV tendency diagnostic~~(Fig. 8b, Fig. 9b). During the second period, around March 21, splitting events take place~~. Furthermore, splitting and merging events in quick succession ~~. The third period occurs from~~ make it hard to fully diagnose the amplitude change. From March 23–24, ~~when~~ the diagnosed tendencies systematically

830 underestimate the decay of the PVA$_{qL}^{-}$. The area of the PVA$_{qL}^{-}$ is very small at this time (not shown), which may make the spatial integration particularly sensitive to the precise location of the boundary. Overall, however, we conclude that the accuracy of our budget evaluation is sufficient and that the diagnosed tendencies presented in the main text reliably represent the relative importance of the different dynamical mechanisms.

835 *Author contributions.* SH developed the quasi-Lagrangian perspective, analyzed the PV dynamics from a quasi-Lagrangian and Lagrangian perspective, and wrote the manuscript. FT calculated and provided the piecewise PV tendencies, developed the Eulerian perspective on the PV dynamics of blocked weather regimes, and contributed to the writing of the manuscript. CMG provided the year-round North Atlantic-European weather regime data based on ERA5. MR contributed to the writing. CMG, MR, and PK gave important guidance during the project and provided feedback on the manuscript.
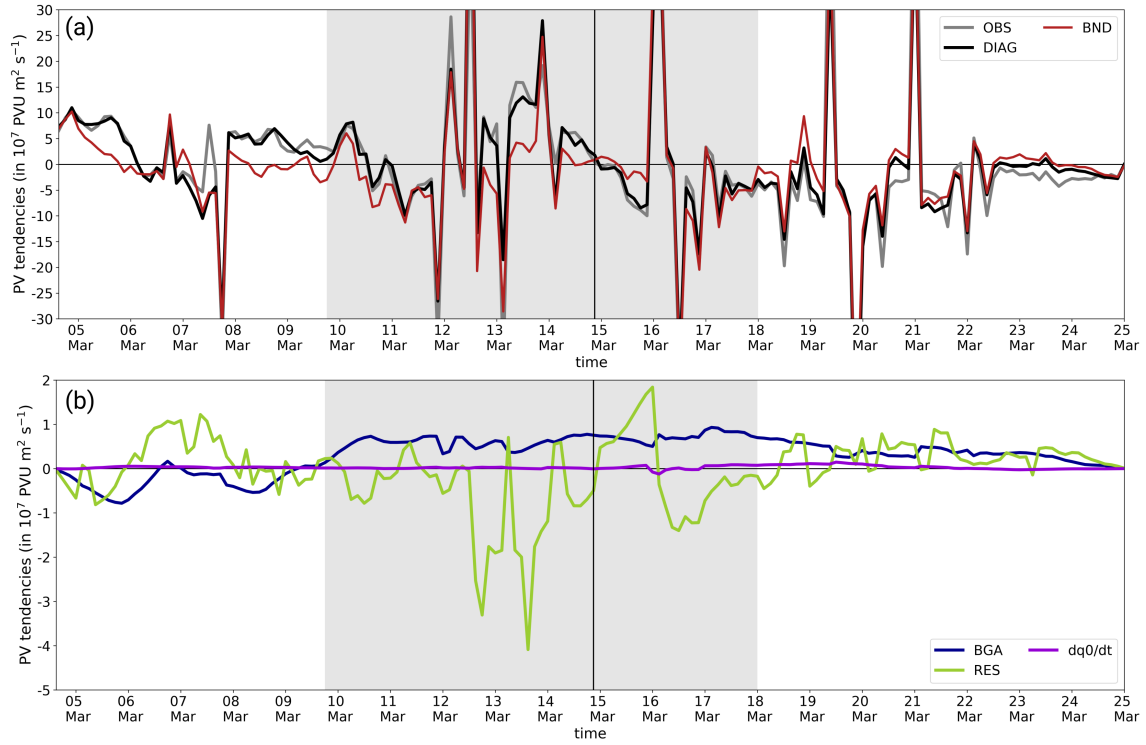
**Figure B1.** ~~Discrepancies between the observed and diagnosed $PVA_{qL}^{-}$ amplitude change.~~ ~~We show the~~ Comparison of observed and diagnosed $PVA_{qL}^{-}$ amplitude change and temporal evolution of remaining PV tendency terms as an addition to Figure 10. (~~black, solid~~a) ~~and~~ Observed amplitude change of the ~~observed~~ $PVA_{qL}^{-}$ (~~black~~OBS, ~~dashed~~grey)$PVA_{qL}^{-}$, full diagnosed amplitude change as of Equation 9 (DIAG, black) and the ~~PV advection~~ boundary term ~~due to the residual~~ (BND, darkred). (b) Remaining terms of Equation 9 that are not contained in ~~the~~ Figure 10: advection of background PV by background wind ~~partition~~ (~~gray~~BGA, ~~solid~~darkblue), advection of background PV by the ~~flux through the $PVA_{qL}^{-}$ boundary~~ residual wind field (~~violet~~RES, yellowgreen) and the ~~flux along~~ local change in the $PVA_{qL}^{-}$ ~~boundary when~~ background PV within the ~~$PVA_{qL}^{-}$ extends north of 80 °N or south of 25 °N~~ 3h-window (~~pink~~$\partial q_0/\partial t$, violet). The grey shading points to the active EuBL regime life cycle ~~of~~ and the vertical line in black indicates where the active EuBL life cycle is ~~shown~~ divided into two for the investigation of the net effect of the tendency terms in ~~gray shading~~Figure 11. Note the different y-axis extends between the panels.

*Competing interests.* MR, PK, and CMG are members of the editorial board of Weather and Climate Dynamics. The authors have no other competing interests to declare.

*Acknowledgements.* The research leading to these results has been done within the sub-project "Dynamics and predictability of blocked regimes in the Atlantic-European region (A8)" of the Transregional Collaborative Research Center SFB / TRR 165 "Waves to Weather" (www.wavestoweather.de) funded by the German Research Foundation (DFG). The contribution of CMG is funded by the Helmholtz Association as part of the Young Investigator Group "Sub-seasonal Predictability: Understanding the Role of Diabatic Outflow" (SPREADOUT, grant VH-NG-1243). We thank the atmospheric dynamics group of ETH Zurich for providing LAGRANTO and three anonymous reviewers whose comments helped to improve the presentation of our results.

# References

Alvarez-Castro, M. C., Faranda, D., and Yiou, P.: Atmospheric Dynamics Leading to West European Summer Hot Temperatures since 1851, Complexity, 2018, https://doi.org/10.1155/2018/2494509, 2018.

Austin, J. F.: The blocking of middle latitude westerly winds by planetary waves, Quarterly Journal of the Royal Meteorological Society, 106, 327–350, https://doi.org/10.1002/qj.49710644807, 1980.

Benedict, J. J., Lee, S., and Feldstein, S. B.: Synoptic view of the North Atlantic Oscillation, Journal of the Atmospheric Sciences, 61, 121–144, https://doi.org/10.1175/1520-0469(2004)061<0121:SVOTNA>2.0.CO;2, 2004.

Buehler, T., Raible, C. C., and Stocker, T. F.: The relationship of winter season North Atlantic blocking frequencies to extreme cold or dry spells in the ERA-40, Tellus A, 63, 212–222, https://doi.org/10.1111/j.1600-0870.2010.00492.x, 2011.

Cassou, C.: Intraseasonal interaction between the Madden-Julian Oscillation and the North Atlantic Oscillation, Nature, 455, 523–527, https://doi.org/10.1038/nature07286, 2008.

Chagnon, J. M., Gray, S. L., and Methven, J.: Diabatic processes modifying potential vorticity in a North Atlantic cyclone, Quarterly Journal of the Royal Meteorological Society, 139, 1270–1282, https://doi.org/10.1002/qj.2037, 2013.

Charney, J.: The Use of the Primitive Equations of Motion in Numerical Prediction, Tellus, 7, 22–26, https://doi.org/10.1111/j.2153-3490.1955.tb01138.x, 1955.

Charney, J. G. and DeVore, J. G.: Multiple Flow Equilibria in the Atmosphere and Blocking, Journal of Atmospheric Sciences, 36, 1205–1216, https://doi.org/10.1175/1520-0469(1979)036<1205:MFEITA>2.0.CO;2, 1979.

Cortesi, N., Torralba, V., Lledó, L., Manrique-Suñén, A., Gonzalez-Reviriego, N., Soret, A., and Doblas-Reyes, F. J.: Yearly evolution of Euro-Atlantic weather regimes and of their sub-seasonal predictability (Climate Dynamics, (2021), 56, 11-12, (3933-3964), 10.1007/s00382-021-05679-y), Climate Dynamics, 56, 3965, https://doi.org/10.1007/s00382-021-05750-8, 2021.

Davis, C. A.: Piecewise Potential Vorticity Inversion, Journal of the Atmospheric Sciences, 49, 1397–1411, https://doi.org/10.1175/1520-0469(1992)049<1397:PPVI>2.0.CO;2, 1992.

Davis, C. A. and Emanuel, K. A.: Potential Vorticity Diagnostics of Cyclogenesis, Monthly Weather Review, 119, 1929–1953, https://doi.org/10.1175/1520-0493(1991)119<1929:PVDOC>2.0.CO;2, 1991.

Davis, C. A., Grell, E. D., and Shapiro, M. A.: The Balanced Dynamical Nature of a Rapidly Intensifying Oceanic Cyclone, Mon. Wea. Rev., 124, 3–26, https://doi.org/10.1175/1520-0493(1996)124<0003:TBDNOA>2.0.CO;2, 1996.

Donat, M. G., Leckebusch, G. C., Pinto, J. G., and Ulbrich, U.: Examination of wind storms over Central Europe with respect to circulation weather types and NAO phases, International Journal of Climatology, 30, 1289–1300, https://doi.org/10.1002/joc.1982, 2010.

Duchon, C. E.: Lanczos Filtering in One and Two Dimensions, Journal of Applied Meteorology and Climatology, 18, 1016–1022, https://doi.org/10.1175/1520-0450(1979)018<1016:LFIOAT>2.0.CO;2, 1979.

Ertel, H.: Ein neuer hydrodynamischer Erhaltungssatz, Die Naturwissenschaften, 30, 543–544, https://doi.org/10.1007/BF01475602, 1942.

Feldstein, S. B.: The dynamics of NAO teleconnection pattern growth and decay, Quarterly Journal of the Royal Meteorological Society, 129, 901–924, https://doi.org/10.1256/qj.02.76, 2003.

Ferranti, L., Corti, S., and Janousek, M.: Flow-dependent verification of the ECMWF ensemble over the Euro-Atlantic sector, Quarterly Journal of the Royal Meteorological Society, 141, 916–924, https://doi.org/10.1002/qj.2411, 2015.

Ferranti, L., Magnusson, L., Vitart, F., and Richardson, D. S.: How far in advance can we predict changes in large-scale flow leading to severe cold conditions over Europe?, Quarterly Journal of the Royal Meteorological Society, 144, 1788–1802, https://doi.org/10.1002/qj.3341, 2018.

Grams, C. M., Wernli, H., Böttcher, M., Čampa, J., Corsmeier, U., Jones, S. C., Keller, J. H., Lenz, C.-J., and Wiegand, L.: The key role of diabatic processes in modifying the upper-tropospheric wave guide: a North Atlantic case-study, Quarterly Journal of the Royal Meteorological Society, 137, 2174–2193, https://doi.org/10.1002/qj.891, 2011.

Grams, C. M., Beerli, R., Pfenninger, S., Staffell, I., and Wernli, H.: Balancing Europe's wind power output through spatial deployment informed by weather regimes, Nature Clim Change, 7, 557–562, https://doi.org/10.1038/nclimate3338, 2017.

Grams, C. M., Magnusson, L., and Madonna, E.: An Atmospheric Dynamics Perspective on the Amplification and Propagation of Forecast Error in Numerical Weather Prediction Models: A Case Study, Quarterly Journal of the Royal Meteorological Society, 144, 2577–2591, https://doi.org/10.1002/qj.3353, 2018.

Grose, W. L. and Hoskins, B. J.: On the Influence of Orography on Large-Scale Atmospheric Flow, Journal of Atmospheric Sciences, 36, 223 – 234, https://doi.org/10.1175/1520-0469(1979)036<0223:OTIOOO>2.0.CO;2, 1979.

Henderson, S. A., Maloney, E. D., and Barnes, E. A.: The influence of the Madden-Julian oscillation on Northern Hemisphere winter blocking, Journal of Climate, 29, 4597–4616, https://doi.org/10.1175/JCLI-D-15-0502.1, 2016.

Hersbach, H., Bell, B., Berrisford, P., Hirahara, S., Horányi, A., Muñoz-Sabater, J., Nicolas, J., Peubey, C., Radu, R., Schepers, D., Simmons, A., Soci, C., Abdalla, S., Abellan, X., Balsamo, G., Bechtold, P., Biavati, G., Bidlot, J., Bonavita, M., De Chiara, G., Dahlgren, P., Dee, D., Diamantakis, M., Dragani, R., Flemming, J., Forbes, R., Fuentes, M., Geer, A., Haimberger, L., Healy, S., Hogan, R. J., Hólm, E., Janisková, M., Keeley, S., Laloyaux, P., Lopez, P., Lupu, C., Radnoti, G., de Rosnay, P., Rozum, I., Vamborg, F., Villaume, S., and Thépaut, J.-N.: The ERA5 global reanalysis, Quarterly Journal of the Royal Meteorological Society, 146, 1999–2049, https://doi.org/10.1002/qj.3803, 2020.

Hong, C.-C., Hsu, H.-H., Lin, N.-H., and Chiu, H.: Roles of European blocking and tropical-extratropical interaction in the 2010 Pakistan flooding, Geophysical Research Letters, 38, https://doi.org/10.1029/2011GL047583, 2011.

Hoskins, B.: A potential vorticity view of synoptic development, Meteorological Applications, 4, 325–334, https://doi.org/10.1017/S1350482797000716, 1997.

Hoskins, B. J., McIntyre, M. E., and Robertson, A. W.: On the Use and Significance of Isentropic Potential Vorticity Maps, Quarterly Journal of the Royal Meteorological Society, 111, 877–946, https://doi.org/10.1002/qj.49711147002, 1985.

Houze, R. A., Rasmussen, K. L., Medina, S., Brodzik, S. R., and Romatschke, U.: Anomalous Atmospheric Events Leading to the Summer 2010 Floods in Pakistan, Bulletin of the American Meteorological Society, 92, 291 – 298, https://doi.org/10.1175/2010BAMS3173.1, 2011.

Illari, L.: A Diagnostic Study of the Potential Vorticity in a Warm Blocking Anticyclone, Journal of Atmospheric Sciences, 41, 3518 – 3526, https://doi.org/10.1175/1520-0469(1984)041<3518:ADSOTP>2.0.CO;2, 1984.

Kautz, L.-A., Martius, O., Pfahl, S., Pinto, J. G., Ramos, A. M., Sousa, P. M., and Woollings, T.: Atmospheric blocking and weather extremes over the Euro-Atlantic sector – a review, Weather and Climate Dynamics, 3, 305–336, https://doi.org/10.5194/wcd-3-305-2022, 2022.

Lavaysse, C., Vogt, J., Toreti, A., Carrera, M. L., and Pappenberger, F.: On the use of weather regimes to forecast meteorological drought over Europe, Natural Hazards and Earth System Sciences, 18, 3297–3309, https://doi.org/10.5194/nhess-18-3297-2018, 2018.

Luo, D., Cha, J., Zhong, L., and Dai, A.: A nonlinear multiscale interaction model for atmospheric blocking: The eddy-blocking matching mechanism, Quarterly Journal of the Royal Meteorological Society, 140, 1785–1808, https://doi.org/10.1002/qj.2337, 2014.

Lupo, A. R.: Atmospheric blocking events: a review, Annals of the New York Academy of Sciences, 1504, 5–24, https://doi.org/10.1111/nyas.14557, 2021.

Madonna, E., Wernli, H., Joos, H., and Martius, O.: Warm Conveyor Belts in the ERA-Interim Dataset (1979-2010). Part I: Climatology and Potential Vorticity Evolution, Journal of Climate, 27, 3 – 26, https://doi.org/10.1175/JCLI-D-12-00720.1, 2014.

925 Magnusson, L.: Diagnostic methods for understanding the origin of forecast errors, Quarterly Journal of the Royal Meteorological Society, 143, 2129–2142, https://doi.org/10.1002/qj.3072, 2017.

Martineau, P., Nakamura, H., Yamamoto, A., and Kosaka, Y.: Baroclinic Blocking, Geophysical Research Letters, 49, e2022GL097 791, https://doi.org/10.1029/2022GL097791, 2022.

Matsueda, M. and Palmer, T. N.: Estimates of flow-dependent predictability of wintertime Euro-Atlantic weather regimes in medium-range

930 forecasts, Quarterly Journal of the Royal Meteorological Society, 144, 1012–1027, https://doi.org/10.1002/qj.3265, 2018.

Methven, J.: Potential vorticity in warm conveyor belt outflow, Quarterly Journal of the Royal Meteorological Society, 141, 1065–1071, https://doi.org/10.1002/qj.2393, 2015.

Michel, C. and Rivière, G.: The link between rossby wave breakings and weather regime transitions, Journal of the Atmospheric Sciences, 68, 1730–1748, https://doi.org/10.1175/2011JAS3635.1, 2011.

935 Michelangeli, P. A., Vautard, R., and Legras, B.: Weather regimes: recurrence and quasi stationarity, https://doi.org/10.1175/1520-0469(1995)052<1237:WRRAQS>2.0.CO;2, 1995.

Miller, D. E. and Wang, Z.: Northern Hemisphere Winter Blocking: Differing Onset Mechanisms across Regions, Journal of the Atmospheric Sciences, pp. 1–38, https://doi.org/10.1175/jas-d-21-0104.1, 2022.

Nakamura, H. and Wallace, J. M.: Observed Changes in Baroclinic Wave Activity during the Life Cycles of Low-Frequency Circulation

940 Anomalies, Journal of Atmospheric Sciences, 47, 1100 – 1116, https://doi.org/10.1175/1520-0469(1990)047<1100:OCIBWA>2.0.CO;2, 1990.

Nakamura, H. and Wallace, J. M.: Synoptic Behavior of Baroclinic Eddies during the Blocking Onset, Monthly Weather Review, 121, 1892 – 1903, https://doi.org/10.1175/1520-0493(1993)121<1892:SBOBED>2.0.CO;2, 1993.

Nakamura, H., Nakamura, M., and Anderson, J. L.: The role of high- and low-frequency dynamics in blocking formation, Monthly Weather

945 Review, 125, 2074–2093, https://doi.org/10.1175/1520-0493(1997)125<2074:TROHAL>2.0.CO;2, 1997.

Nakamura, N. and Huang, C. S. Y.: Atmospheric blocking as a traffic jam in the jet stream, Science, 361, 42–47, https://doi.org/10.1126/science.aat0721, 2018.

Petoukhov, V., Rahmstorf, S., Petri, S., and Schellnhuber, H. J.: Quasiresonant amplification of planetary waves and recent Northern Hemisphere weather extremes, Proceedings of the National Academy of Sciences, 110, 5336–5341, https://doi.org/10.1073/pnas.1222000110,

950 2013.

Pfahl, S. and Wernli, H.: Quantifying the relevance of atmospheric blocking for co-located temperature extremes in the Northern Hemisphere on (sub-)daily time scales, Geophysical Research Letters, 39, https://doi.org/10.1029/2012GL052261, 2012.

Pfahl, S., Schwierz, C., Croci-Maspoli, M., Grams, C. M., and Wernli, H.: Importance of latent heat release in ascending air streams for atmospheric blocking, Nature Geoscience, 8, 610–614, https://doi.org/10.1038/ngeo2487, 2015.

955 Quinting, J. F. and Grams, C. M.: EuLerian Identification of ascending AirStreams (ELIAS 2.0) in numerical weather prediction and climate models – Part 1: Development of deep learning model, Geoscientific Model Development, 15, 715–730, https://doi.org/10.5194/gmd-15-715-2022, 2022.

Rex, D. F.: Blocking Action in the Middle Troposphere and its Effect upon Regional Climate, Tellus, 2, 196–211, https://doi.org/10.1111/j.2153-3490.1950.tb00331.x, 1950.

960  Rossby, C.-G.: Planetary flow patterns in the atmosphere, 1940.

Röthlisberger, M., Martius, O., and Wernli, H.: Northern Hemisphere Rossby Wave Initiation Events on the Extratropical Jet—A Climatological Analysis, J. Climate, 31, 743–760, https://doi.org/10.1175/JCLI-D-17-0346.1, 2018.

Schwierz, C., Croci-Maspoli, M., and Davies, H. C.: Perspicacious indicators of atmospheric blocking, Geophysical Research Letters, 31, https://doi.org/10.1029/2003GL019341, 2004.

965  Shutts, G. J.: The propagation of eddies in diffluent jetstreams: Eddy vorticity forcing of 'blocking' flow fields, Quarterly Journal of the Royal Meteorological Society, 109, 737–761, https://doi.org/10.1002/qj.49710946204, 1983.

Sillmann, J., Croci-Maspoli, M., Kallache, M., and Katz, R. W.: Extreme Cold Winter Temperatures in Europe under the Influence of North Atlantic Atmospheric Blocking, Journal of Climate, 24, 5899 – 5913, https://doi.org/10.1175/2011JCLI4075.1, 2011.

Sprenger, M. and Wernli, H.: The LAGRANTO Lagrangian analysis tool - Version 2.0, Geoscientific Model Development, 8, 2569–2586, 
970  https://doi.org/10.5194/gmd-8-2569-2015, 2015.

Steinfeld, D. and Pfahl, S.: The Role of Latent Heating in Atmospheric Blocking Dynamics: A Global Climatology, Climate Dynamics, https://doi.org/10.1007/s00382-019-04919-6, 2019.

Teubler, F. and Riemer, M.: Dynamics of Rossby Wave Packets in a Quantitative Potential Vorticity–Potential Temperature Framework, Journal of the Atmospheric Sciences, 73, 1063–1081, https://doi.org/10.1175/JAS-D-15-0162.1, 2016.

975  Teubler, F. and Riemer, M.: Potential-Vorticity Dynamics of Troughs and Ridges within Rossby Wave Packets during a 40-Year Reanalysis Period, Weather and Climate Dynamics, 2, 535–559, https://doi.org/10.5194/wcd-2-535-2021, 2021.

Teubler, F., Riemer, M., Polster, C., Grams, C. M., Hauser, S., and Wirth, V.: Similarity and variability of blocked weather-regime dynamics in the Atlantic-European region, Weather and Climate Dynamics Discussions, 2022, 1–31, https://doi.org/10.5194/wcd-2022-56, https://wcd.copernicus.org/preprints/wcd-2022-56/, 2022.

980  Vautard, R.: Multiple weather regimes over the North Atlantic: analysis of precursors and successors, https://doi.org/10.1175/1520-0493(1990)118<2056:MWROTN>2.0.CO;2, 1990.

Vitart, F., Robertson, A. W., and Anderson, D. L. T.: Sub-seasonal to seasonal prediction: The gap between weather and climate forecasting, Sub-seasonal to Seasonal Prediction: The Gap Between Weather and Climate Forecasting, 61, 1–585, https://doi.org/10.1016/C2016-0-01594-2, 2012.

985  Wernli, H.: A Lagrangian-based analysis of extratropical cyclones. II: A detailed case-study, Quarterly Journal of the Royal Meteorological Society, 123, 1677–1706, https://doi.org/10.1002/qj.49712354211, 1997.

Wirth, V., Riemer, M., Chang, E. K., and Martius, O.: Rossby wave packets on the midlatitude waveguide-A review, Monthly Weather Review, 146, 1965–2001, https://doi.org/10.1175/MWR-D-16-0483.1, 2018a.

Wirth, V., Riemer, M., Chang, E. K. M., and Martius, O.: Rossby Wave Packets on the Midlatitude Waveguide—A Review, Monthly Weather 
990  Review, 146, 1965–2001, https://doi.org/10.1175/MWR-D-16-0483.1, 2018b.

Woollings, T., Barriopedro, D., Methven, J., Son, S. W., Martius, O., Harvey, B., Sillmann, J., Lupo, A. R., and Seneviratne, S.: Blocking and its Response to Climate Change, Current Climate Change Reports, 4, 287–300, https://doi.org/10.1007/s40641-018-0108-z, 2018.

Yamazaki, A. and Itoh, H.: Selective absorption mechanism for the maintenance of blocking, Geophysical Research Letters, 36, 4–7, https://doi.org/10.1029/2008GL036770, 2009.

995   Yiou, P. and Nogaj, M.: Extreme climatic events and weather regimes over the North Atlantic: When and where?, Geophysical Research Letters, 31, https://doi.org/10.1029/2003GL019119, 2004.

Zierl, B. and Wirth, V.: The Influence of Radiation on Tropopause Behavior and Stratosphere-Troposphere Exchange in an Upper Tropospheric Anticyclone, Journal of Geophysical Research: Atmospheres, 102, 23 883–23 894, https://doi.org/10.1029/97JD01667, 1997.